Eidgenössische Technische Hochschule Zürich
Swiss Federal Institute of Technology Zurich

# High-Q development and qubit manipulations in a 3D circuit QED architecture

Master's Thesis in Physics
Presented by Kristinn Juliusson
Supervised by Dr. Johannes Fink
Handed in to Prof. Dr. Andreas Wallraff,
Laboratory for Solid State Physics, ETH Zurich

Zurich, April 26, 2012

*For my left hand.*

**Abstract**

Superconducting qubits are one of the most promising implementations of a quantum information processor. Though this particular approach has the advantage of fast operation times it is still limited by coherence times, which until recently were about $1\mu s$. A great improvement in lifetimes was observer by putting a superconducting qubit into a high-Q 3D cavity [1] with T1 and T2 up to 60 $\mu s$ and 20 $\mu s$ respectively. In this thesis we develop our own 3D cavity with $Q_{\text{int}} = 2 \cdot 10^6$. We characterize 4 qubits in a cavity with $Q_{\text{int}} = 2 \cdot 10^5$ and observe T1 and T2 up to 14.7 and 9.1 $\mu s$ respectively. We drive both single and two tone blue sideband transitions and analyze them for implementing a controlled NOT scheme on a two qubits sample. Fixed coupling is observed between the qubits and is used to implement a controlled-Z gate with 67% process fidelity.

# Contents

# 1 Introduction

## 1.1 The idea of quantum information processing

In 1937 the mathematician Alan Turing published a paper on what is today known as the Turing machine [2]. This abstract theory stated what is now known as the Church-Turing thesis, namely that any information processing achievable on a physical system can also be efficiently accomplished with the Turing machine. The importance of the Turing machine for the modern community is crystallized in the fact that the personal computer, which is essential in the daily lives of most people in the western world, is based on the Turing machine. Physicists, however, had great difficulties in using classical computers to simulate quantum systems. This lead Richard Feynman [3] to suggest in the 1980's that in order to simulate a quantum mechanical system a computer based on the laws of quantum mechanics is needed. The Church Turing thesis was put to the test a few years later by David Deutsch [4]. Since the Church-Turing machine is based on the laws of computer science, Deutsch claimed that a more general theory, one based on the laws of physics instead of computer science, could be developed. With such a theory any physical system could be simulated.

Let us now compare the classical computer to the quantum one. Classically all operations are based on discrete binary logic where bits are either 0 or 1. In todays computers these bits are represented by transistors. A quantum mechanical bit or qubit can be in a superposition of 0 and 1 i.e. it is 0 with a non-zero probability x and 1 with probability 1-x. This feature distinguishes the quantum computer from the classical one. There are indeed various physical implementations of qubits, however, a spin subspace of a spin 1/2 particle is the canonical example of such a system.

Although still not proven, there are strong indicators that the quantum computer violates the Church-Turing thesis and by doing so break down fundamental barriers of classical computer science. To name two of those indicators we first mention Shors' factorizing algorithm. In 1994 Peter Shor published a paper [5] where he had developed an algorithm for a quantum computer that could factorize a number to its prime integers in a polynomial time, a task believed to be only possible in an exponential time with a classical computer. The significance of Shor's algorithm is emphasized by the fact that the common way of encrypting information is based on factorizing a large number. Secondly we mention Grovers' algorithm [6] which searches through an unstructured space faster than a classical computer.

Both algorithms have been implemented. At IBM nuclear magnetic resonance (NMR) of a molecule was used in 2001 as a 7 qubit quantum computer to factorize 15 into 3 and 5 using Shor's algorithm [7]. Even though NMR meets the criteria for a quantum bit [8] very well on todays standard it requires complicated control sequences of multi-qubit systems due to their permanent coupling [9]. Other implementations for quantum information processing are e.g. quantum dots [10], NV centers [11] and photons [12] which due to their noise resistance and low-loss fibers are often used in quantum communication

schemes [13]. The most advanced implementation to date is based on trapped ions where up to 14 qubits have been entangled [14]. The qubit implementation in the work presented here is however with superconducting circuits. Even though it has not gained coherent control over the same number of qubits it has great potential for scaling thanks to advanced fabrication techniques.

## 1.2 Implementation in circuit QED

Ever since Nakamura observed coherent dynamics of a superconducting circuit [15] the field of superconducting qubits has become a popular research topic. Significant progress was made by Blais [16] and Wallraff [17] who coupled a coplanar waveguide to a charge qubit and observed single photon interaction. This sparked off the field of circuit quantum electrodynamics(circuit QED). Milestones such as high fidelity qubit readout [18], observation of vacuum Rabi oscillations [19] [20] and sideband transitions [21] with a single qubit-resonator samples was already accomplished in 2007. Since then both two [22] and three qubit states have been observed [23] and used for logical 3 qubit operations [24] in superconducting circuits.

The strength of this particular implementations is the possibility of fast qubit operation, i.e. a few nanoseconds, and potential for scalability. Since superconducting qubits are macroscopic they do not easily have long lifetimes [25]. Even though it has gone from a few nanoseconds to about a microsecond in less than a decade it remains as one of the main hurdles in the development of the superconducting quantum computer. In 2011 Paik et.al.[1] observed a significant improvement in lifetimes by coupling a qubit to a 3D cavity resonator. They measured an energy relaxation time of up to 60 $\mu s$ and a dephasing time of up to 20 $\mu s$. Various control techniques such as gate lines, flux lines and flux coils [26, 17] are used for qubit control in 2D circuit QED. These techniques have not been implemented in 3D cavities and thus present a draw back from on-chip samples. By adapting these techniques and gaining the same qubit control for 3D cavities its long coherence times can be exploited for unprecedented fidelities in quantum information processing in circuit QED. This is the inspiration for the experiments in this thesis.

The thesis is divided into two main chapters, Theory and Experiment. A running theme through both of them is to discuss first the cavity itself, then we talk about single qubits and its characterization and finally discuss two qubit effects and operations.

# 2 Theory

The work presented here is well supported by theory. The cavities are well understood from electrodynamics and electrical engineering, the qubits from the Josephson effect and the resonator-qubit interaction from quantum optics.

We begin by discussing the theory of electric fields and resonances in 3D cavities and resonator transmission in an electrical circuit. We then talk about the quantization of an LC circuit. From there we proceed to show how an artificial atom is implemented in such a circuit by introducing a Josephson junction and how a 2 level subspace of the artificial atom can be defined as a qubit. We then explain the abstract theory of a qubit in a two dimensional Hilbert space and introduce the spin 1/2 notation and the Bloch sphere commonly used in the field of quantum information. After having discussed the qubit and the resonator separately we introduce a system where a qubit is coupled to a resonator and describe it with the Jaynes-Cummings model(JC model) from the field of quantum optics. In order to understand the qubit manipulation system we next add electromagnetic drive field and combine it with JC model. Thereafter we describe sideband transitions on the joint qubit-resonator system and then conclude the chapter by discussing two qubit gates.

## 2.1 3D Cavity resonator

### 2.1.1 Solving Maxwell's equations for a 3D cavity resonator

A cavity resonator can be understood from Maxwell's equations in a tree dimensional rectangular geometry. By setting the boundary conditions for the electric and magnetic field to $E_\perp = 0$ and $B_\parallel = 0$ respectively, corresponding to a perfect conductor, we solve the equations($\perp$ stands for the component perpendicular to the surface and $\parallel$ for the parallel one). The solution obtained from ref. [27] is derived from an electromagnetic wave traveling along a rectangular

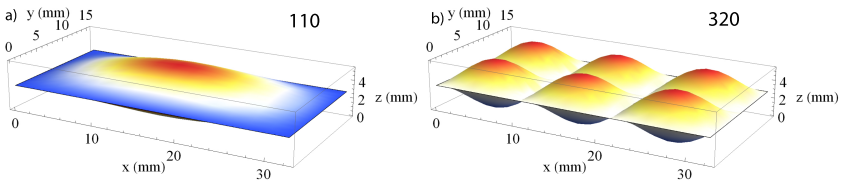


Figure 1: $E_z$ distributions in a cavity resonator for a) the first mode (1,1,0) and b) the sixth mode (3,2,0).

waveguide and the direction of propagation is defined as z

$$\begin{aligned} E_z &= E_0 \sin\left(\frac{n\pi}{a}x\right)\sin\left(\frac{m\pi}{b}y\right)\cos\left(\frac{p\pi}{d}z\right) \\ E_x &= -\frac{E_0}{h^2}\left(\frac{p\pi}{d}\right)\left(\frac{m\pi}{a}\right)\cos\left(\frac{n\pi}{a}x\right)\sin\left(\frac{m\pi}{b}y\right)\sin\left(\frac{p\pi}{d}z\right) \\ E_y &= -\frac{E_0}{h^2}\left(\frac{p\pi}{d}\right)\left(\frac{n\pi}{b}\right)\sin\left(\frac{n\pi}{a}x\right)\cos\left(\frac{m\pi}{b}y\right)\sin\left(\frac{p\pi}{d}z\right). \end{aligned} \tag{2.1}$$

Here a, b and d are the dimensions along the x, y and z axes respectively and n, m and p (all positive integers) are the mode corresponding indicies. The prefactor $h$ depends on the frequency, $\nu = \omega/2\pi$, as $h^2 \propto \omega^2$.

The resonance frequencies are given by

$$\nu_r = \frac{c}{2\pi\sqrt{\mu_r\epsilon_r}}\sqrt{\left(\frac{n\pi}{a}\right)^2 + \left(\frac{m\pi}{b}\right)^2 + \left(\frac{p\pi}{d}\right)^2}. \tag{2.2}$$

From Equation 2.1 we can see that only one mode index can be zero in order to have a non zero electric field and the cavity. Equation 2.2 tells us that by assuming $d < a, b$ the first mode is the (n,m,p)=(1,1,0) mode. For all cases where $p = 0$ we have only a $E_z$ component of the electric field i.e.

$$\begin{aligned} E_z &= E_0 \sin\left(\frac{n\pi}{a}x\right)\sin\left(\frac{m\pi}{b}y\right) \\ \nu_r &= \frac{c}{2\pi\sqrt{\mu_r\epsilon_r}}\sqrt{\left(\frac{n\pi}{a}\right)^2 + \left(\frac{m\pi}{b}\right)^2}. \end{aligned} \tag{2.3}$$

The (n,m,0) modes can be visualized as the number of antinodes along a given axis. In Figure 1 a and b one can see a plot of the (1,1,0) and the (3,2,0) modes in the x-y plane for a box with the dimensions a=32mm, b=15.5mm and d=5mm. The electric field distribution is independent of z.

### 2.1.2 Quality factors

A useful analogy of the cavity described above is a Fabri-Perot resonator where a photon is reflected between two parallel mirrors, see Figure 2 a. The photon will eventually decay. Either trough the mirrors are if they are not perfectly reflecting or by interacting via interaction inside the cavity. We thus assign a decay rate $\kappa$ to the cavity. A quality factor, Q, can be thought of as the average number of oscillations between the two mirrors before a photon decays.

In circuit theory we look at the cavity as an LC oscillator where ideally the photon resonates forever, see Figure 2 b. In reality however it will eventually dissipate via the conductance $G$, which is the inverse of the resistance $R$, $G = 1/R$. A quality factor for a cavity is thus defined as [29, 30]

$$Q_{\mathrm{int}} = \frac{2\pi\nu_{\mathrm{r}}C}{G_{\mathrm{int}}}, \tag{2.4}$$

where $C$ is the circuit capacitance and $G_{\text{int}}$ represents the loss in the cavity. In realistic system the cavity is a part of a bigger circuit. Losses outside the cavity, $G_{\text{ext}}$, give therefore rise to a finite

$$Q_{\text{ext}} = \frac{2\pi\nu_{\text{r}}C}{G_{\text{ext}}}. \tag{2.5}$$

We define the quality factor of the total circuit, called the loaded $Q$, as

$$Q_L = \frac{1}{\frac{1}{Q_{\text{int}}} + \frac{1}{Q_{\text{ext}}}}. \tag{2.6}$$

When measuring the quality factors of a cavity we must therefore look at it as a part of a circuit. The transmission loss through the cavity in the vicinity of a resonance peak follows a Lorentzian shape

$$S(\nu) = \frac{S_{\max}}{1 + (\frac{\nu - \nu_r}{\delta\nu_r})^2}, \tag{2.7}$$

where $\nu_r$ is the resonance frequency $\delta\nu_r$ is half the bandwidth at -3dB and $S_{\max}$ is the transmission signal at the resonance frequency $S(\nu_r)$, see Figure 3.

$Q_{\text{L}}$ can be determined from such a transmission spectroscopy, $Q_{\text{L}} = \frac{\nu_{\text{r}}}{2\delta\nu_{\text{r}}}$. If we have symmetric coupling we can determine $Q_{\text{int}}$ from the insertion loss $\beta$ which is expressed in dB. It must be converted into the units of $S(\nu)$ i.e. $S_(\nu_{\text{r}}) = 10^{\frac{\beta}{10}}$ for Watts or $S_(\nu_{\text{r}}) = 10^{\frac{\beta}{20}}$ for amplitude. One can then calculate

$$Q_{\text{int}} = \frac{Q_{\text{L}}}{1 - S(\nu_{\text{r}})}. \tag{2.8}$$

Having determined $Q_{\text{int}}$ and $Q_{\text{L}}$ one can calculate $Q_{\text{ext}}$ from Equation 2.6. Figure 3 b shows the sum of the Lorentzian resonance peaks up to 20 GHz for the dimensions which we use (a=32mm, b=15.5mm and d=5mm). All resonances, $\nu_r$, where $p \neq 0$ are above 20 GHz.

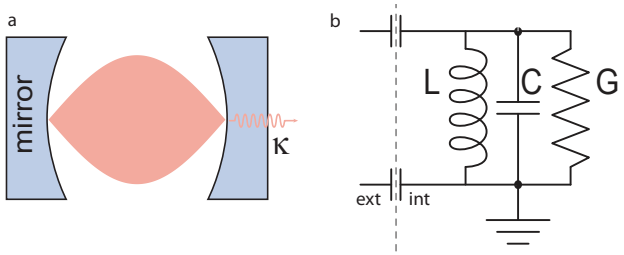


Figure 2: a) In a Fabri Perot resonator photons oscillate between two mirrors. The loss of photons out of the cavity at the rate $\kappa$ gives rise to a finite quality factor (adapted from [28]). b) An analogous setup in electric circuits is a lumped element resonator. It is capacitively coupled to the environment, providing a photon input/decay channel. This we call loading of the circuit.

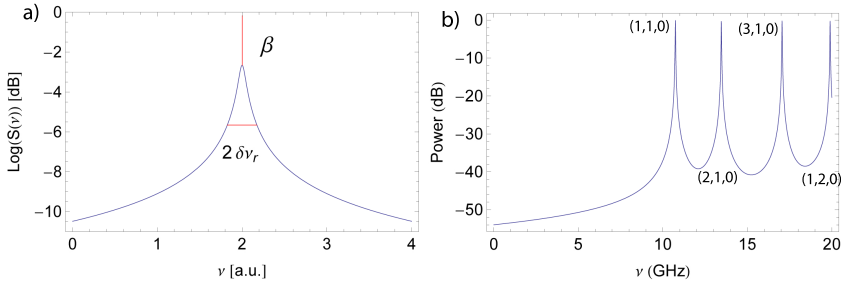


Figure 3: a)The shape of a Lorentzian peak. The resonance frequency $\nu_r$ and $\delta\nu_r$ are used to calculate the loaded Q. The insertion loss $\alpha$ is used to calculate both the internal and the external Q. b) The transmission spectrum of all resonance up to 20 GHz for the dimensions $a, b, c = 32, 15.5, 5mm$.

### 2.1.3 Quantizing an LC circuit

A cavity resonator can be represented as an LC electric circuit where a capacitor with the capacitance $C$ and an inductor with the self-inductance $L$ are connected in series [31]. Assuming zero resistance this system is a harmonic oscillator with the angular frequency $\omega = \frac{1}{\sqrt{LC}}$ and a Hamiltonian

$$H = \frac{\phi^2}{2L} + \frac{q^2}{2C}, \tag{2.9}$$

where $q$ is the charge on the capacitor and $\phi$ is the induced magnetic flux in the inductor. This Hamiltonian can be quantized and rewritten in terms of the ladder operators $\hat{a}^\dagger$ and $\hat{a}$

$$\hat{H} = \frac{\hat{\phi}^2}{2L} + \frac{\hat{q}^2}{2C} = \hbar\omega(\hat{a}^\dagger\hat{a} + \frac{1}{2}) \tag{2.10}$$

with the commutation relation $[\hat{\phi}, \hat{q}] = i\hbar$.

## 2.2 Superconducting qubits

### 2.2.1 Josephson junction

By introducing a non-linear element into the harmonic LC circuit it becomes anharmonic. In such a system two levels with a unique energy separation can represent our qubit. We thus introduce a Josephson junction to replace the inductor. The junction is a thin layer of a non-conducting material between two superconductors, through which cooper pairs can tunnel [31, 32]. The voltage and current through the junction is given as

$$I = I_c \sin(\delta) \quad \text{and} \quad V = \frac{\phi_0}{2\pi}\frac{\partial\delta}{\partial t} \tag{2.11}$$

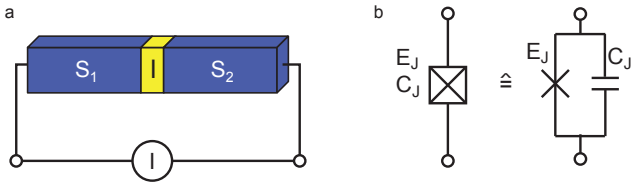


Figure 4: a) A Josephson junction comprises two superconducting leads ($S_1$,$S_2$) separated by a thin insulating barrier ($I$) through which Cooper pairs can tunnel. b) Josephson junction in a circuit diagram. The symbol for a Josephson junction in circuit diagrams is an x. The inherent capacitance between the two leads, parallel to the junction is represented by a box drawn around the x.(Taken from [28])

where $I_c$ is the critical current through the junction, $\delta$ is the phase difference between the cooper pairs on each side of the junction and $\phi_0 = \frac{h}{2e}$ is the flux quantum. By using the law of inductance $V = -L\frac{\partial I}{\partial t}$ we can extract the non-linear inductance of the Josephson junction

$$L = \frac{\phi_0}{2\pi I_c \cos(\delta)}. \tag{2.12}$$

The Josephson junction introduces a non-linear inductance in our circuit. This results in an anharmonic energy level spectrum which can be compared to that of an atom. By isolating two levels we can define a qubit.

### 2.2.2 Cooper pair box

The information in the circuit corresponding to 0 or 1 in binary language is stored in the variables $\hat{\phi}$ or $\hat{q}$. For $\phi$ it corresponds to which direction the flux flows through the circuit and for $q$ on which side of the capacitor the charge sits. In addition one can use the phase which is related to the flux as$\phi = \frac{\phi_0 \delta}{2\pi}$.

The qubit used in our experiments is a charge qubit called transmon. In order to understand its function it is helpful to take a look at its predecessor, the Cooper pair box(CPB).

Figure 5 shows a circuit diagram of a Cooper pair box. The part of the circuit enclosed by the dotted line is a superconducting island. The state of the qubit is then defined by the number of excess Cooper pairs on the island.

The qubit energy can be divided into two parts; inductive energy, $E_1$, in Josephson junction and capacitive energy $E_2$. The inductive energy in the junction is defined as $E_1(t) = -E_J \cos(\frac{2\pi\phi(t)}{\phi_0})$, where $E_J = \frac{\phi_0 I_C}{2\pi}$ is called the Josephson energy. The capacitive energies combine to give $E_2 = E_C(n - n_g)^2$ where $E_C = \frac{(2e)^2}{2C_\Sigma}$ is called the charging energy and $C_\Sigma$ is the total capacitance of the island to the rest of the circuit. Here $n$ is the integer number of excess

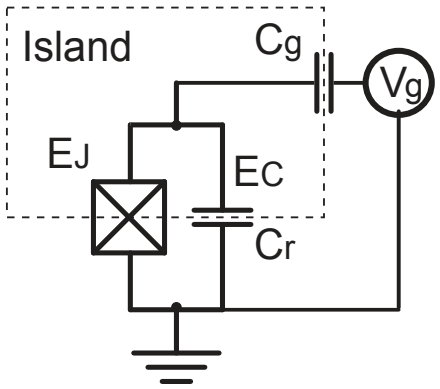


Figure 5: Cooper pair Box. A superconducting island is capacitively coupled to all the near by metallic structures. Cooper pairs tunnel to and from the island through a Josephson junction. The number of Cooper pairs in the island can be controlled by tuning the gate voltage $V_g$.

pairs on the island and $n_g$ is a continuous variable called the gate charge and is tuned by the voltage over the gate capacitor. The Hamiltonian is thus

$$H = E_C(n - n_g)^2 - E_J cos(\delta). \tag{2.13}$$

The CPB is designed such that $E_J \simeq E_C$.

A quantized version of the Hamiltonian 2.13 can write in the basis of the canonical variables $n \to \hat{n}$, or $\delta \to \hat{\delta}$. By choosing the charge basis we get [33]

$$\hat{H} = E_C \sum_n (\hat{n} - n_g)^2 \left|n\right\rangle \left\langle n\right| - \frac{E_J}{2} \sum_n (\left|n\right\rangle \left\langle n+1\right| + \left|n+1\right\rangle \left\langle n\right|), \tag{2.14}$$

with the relations $[\hat{\delta}, \hat{n}] = i$ and $e^{\pm i\hat{\delta}} \left|n\right\rangle = \left|n \pm 1\right\rangle$.

### 2.2.3 Transmon qubit

The energy levels $E_\mathrm{l}$ of the Hamiltonian in Equation 2.14 can be calculated numerically without any approximations [28]. Figure 6 shows calculated energy levels for 3 different values of $E_\mathrm{J}/E_\mathrm{C}$. Figure 6 a and b represent the CPB regime where the dependence of $E_\mathrm{l}$ on $n_\mathrm{g}$ leaves the CPB vulnerable to charge noise. In the limit $E_\mathrm{J} \gg E_\mathrm{C}$ The energy dispersion of level l can be approximated as [34]

$$\epsilon_\mathrm{l} = E_\mathrm{l}(1/2) - E_\mathrm{l}(0) \propto e^{\sqrt{E_\mathrm{J}/E_\mathrm{C}}} \tag{2.15}$$

demonstrating that by increasing the ratio $E_\mathrm{J}/E_\mathrm{C}$ on can reduce the dispersion. Figure 2.14 shows that by increasing the ratio from 1 to 50 the charge noise

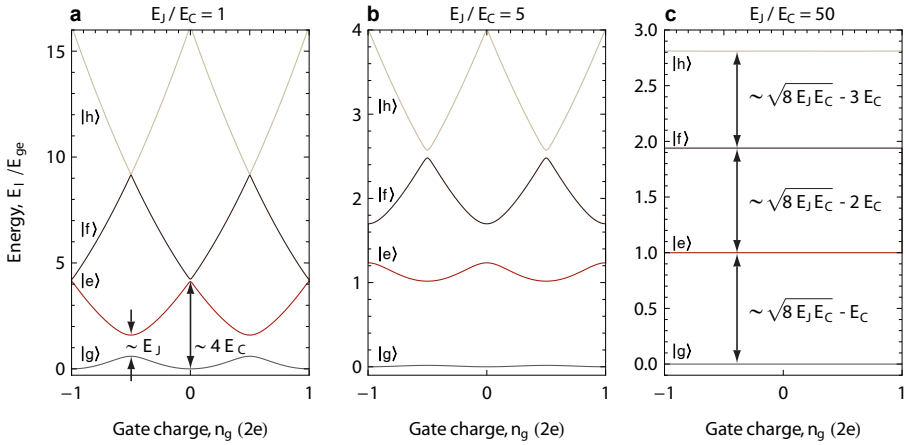


Figure 6: Numerical solution of the charge qubit Hamiltonian in Equation 2.14. By increasing $E_J/E_C$ we can decrease the qubits sensitivity to charge noise. The energy levels are given in units of $E_l/E_{ge}(l = g, e, f, h)$, where $E_{ge}$ is evaluated at $n_g = 0.5$. (Figures taken from [28])

sensitivity is significantly reduced. This alteration comes at a price however as the anharmonicity, $\alpha = E_{12} - E_{01}$ where $E_{\mathrm{nm}} = E_{\mathrm{m}} - E_{\mathrm{n}}$, is comparatively lower. Though the value $\alpha \approx -E_{\mathrm{C}}$ relative to the first excitation energy $E_{01}$ it behaves as

$$\frac{\alpha}{E_{01}} \approx -\sqrt{\frac{8E_{\mathrm{J}}}{E_{\mathrm{C}}}} \tag{2.16}$$

and is thus reduced as $E_J/E_C$ is increased. This results in a lower limit on pulse lengths used for qubit operations. A charge qubit with $E_{\mathrm{J}} \gg E_{\mathrm{C}}$ is called a transmon.

## 2.3 Qubit theory - The Bloch sphere

Having now discussed how an artificial atom can be implemented with a superconducting circuit we proceed by defining a qubit as a two level subspace of such an atom. This will lead us into the generic behavior of qubits.

We can write the Hamiltonian in Equation 2.14 in its eigen basis as

$$\hat{H} = \hbar \sum_i \omega_i \left|i\right\rangle \left\langle i\right| . \tag{2.17}$$

By restricting ourselves to the lowest two eigenstates we effectively realize a two level system or equivalently a qubit. The basis states of the qubit, $|g\rangle$ and $|e\rangle$, can be represented as

$$|g\rangle = \begin{pmatrix} 1 \\ 0 \end{pmatrix} \quad |e\rangle = \begin{pmatrix} 0 \\ 1 \end{pmatrix}. \tag{2.18}$$

and the Hamiltonian can be written as

$$\hat{H} = \hbar\omega_{ge}\hat{\sigma}_z \tag{2.19}$$

where $\hat{\sigma}_z$ is the Pauli z operator and $\omega_{ge}/2\pi$ is the excitation frequency of the qubit.

The generic state of a qubit can be represented as a 2x2 matrix called a density matrix $\rho$, which has the following criteria: A matrix with trace 1, Hermitian and positive-semidefinite. A more visual representation of a qubit state is as a vector originating at the center of a unit sphere. This sphere is called the Bloch sphere and the vector a Bloch vector [35]. As seen in Figure 7 the variable $\theta$ represents the longitudinal angle and $\phi$ the azimuthal angle. The

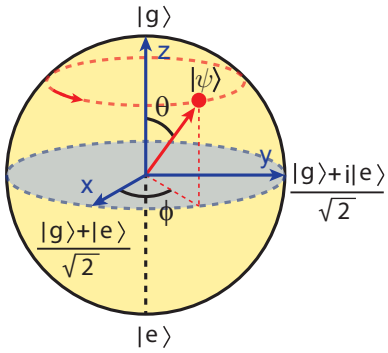


Figure 7: A spin 1/2 particle is represented as a vector on the Bloch sphere. At the equator we have the equal superposition states $|+\rangle, |-\rangle$ and $|\circlearrowleft\rangle, |\circlearrowright\rangle$ which correspond to $(|g\rangle \pm |e\rangle)/\sqrt{2})$ and $|g\rangle \pm i\,|e\rangle\,/\sqrt{2})$.

relation between the density matrix $\rho$ and the Bloch vector $\vec{r} = (r_x, r_y, r_z)$ is given as

$$\rho = \frac{1}{2}(\mathbb{1} + \vec{r}\cdot\vec{\sigma}), \tag{2.20}$$

where $\vec{\sigma} = (\hat{\sigma}_{\mathrm{x}}, \hat{\sigma}_{\mathrm{y}}, \hat{\sigma}_{\mathrm{z}})$ are the Pauli matrices and $\mathbb{1}$ is the identity.

When the Pauli matrices, $\hat{\sigma}_{\mathrm{x}}, \hat{\sigma}_{\mathrm{y}}, \hat{\sigma}_{\mathrm{z}}$, are exponentiated $e^{\hat{\sigma}_{\mathrm{x,y,z}}}$ they define operations, $R_{\mathrm{x}}$, $R_{\mathrm{y}}$, $R_{\mathrm{z}}$ which rotate the state about the respective axis on the bloch sphere

$$\begin{gathered} R_x = \begin{pmatrix} \cos(\theta/2) & -i\sin(\theta/2) \\ i\sin(\theta/2) & \cos(\theta/2) \end{pmatrix} R_y = \begin{pmatrix} \cos(\theta/2) & -\sin(\theta/2) \\ \sin(\theta/2) & \cos(\theta/2) \end{pmatrix} \\ R_z = \begin{pmatrix} e^{i\theta/2} & 0 \\ 0 & e^{i\theta/2} \end{pmatrix}. \end{gathered} \tag{2.21}$$

A Pauli matrix in a Hamiltonian represents a rotation about the same axis as its corresponding $R$ matrix. Expanding to a system of two qubits, A and B, is

represented as 4x4 density matrix $\rho_{2q} \in \mathbb{C}_a \otimes \mathbb{C}_b = \mathbb{C}^2$. In the 2 qubit case, however, the visualization of the state analogous to the Bloch sphere is not possible in the same way.

Qubit states can be divided into pure states and mixed states. A pure state contains all its information and can be written in the basis in Equation 2.18 as

$$|\psi\rangle = \alpha |g\rangle + \beta |e\rangle , \quad |\alpha| + |\beta| = 1 \tag{2.22}$$

where $\alpha, \beta \in \mathbb{C}$ and $|\psi\rangle$ in a 2-dimensional complex vector space. The density matrix of a pure state can be written as

$$\rho = |\psi\rangle \langle\psi| = \begin{pmatrix} \alpha^2 & \alpha\beta \\ \alpha^*\beta^* & \beta^2 \end{pmatrix}. \tag{2.23}$$

In the Bloch picture a pure state resides on the surface of the sphere. Equation 2.19 can then be rewritten onto the form

$$\hat{H} = \cos\left(\frac{\theta}{2}\right) |g\rangle + e^{i\phi} \sin\left(\frac{\theta}{2}\right) |e\rangle \tag{2.24}$$

where we have omitted an irrelevant total global phase.

Mixed states have lost some of their information out into the environment and can thus not be represented as normalized vectors complex as in equation 2.22. A a Bloch vector, a mixed state lies inside the sphere and has a length $|\vec{r}| < 1$. The state where $|\vec{r}| = 0$ is called the maximally mixed state.

## 2.4 The generalized Jaynes-Cummings model

Having discussed a resonator and a qubit separately we now look at a system with a dipole coupling between a transmon and a resonator.

The generalized Jaynes-Cummings model is used to describe the transmon-resonator interaction [36, 34]. The Hamiltonian is

$$\hat{H} = \hbar \sum_l \omega_l |l\rangle \langle l| + \hbar\omega_r \hat{a}^\dagger \hat{a} + \left( \hbar \sum_l g_{l,l+1} |l\rangle \langle l+1| \hat{a}^\dagger + H.c. \right) \tag{2.25}$$

where the joint transmon-resonator eigenstates are denoted as $|ln\rangle$ where $l = g, e, f...$ are the transmon states (notation: $g + 1 = e, e + 1 = f$ etc.) and $n = \langle \hat{a}^\dagger \hat{a} \rangle = 0, 1, 2...$ is the number of photons in the resonator. The first term in Equation 2.25 represents the transmon energy, the second one the resonator energy and the third takes into account the coupling of the dipole moment of the qubit, d, to the electric field, E, in the cavity $\hbar g_{01} = dE_{\text{rms}}$[16]. Effectively, this coupling is however calculated as [34]

$$\hbar g_{l,l+1} = 2e\beta V^0_{rms} \langle l| \hat{n}_c |l+1\rangle \tag{2.26}$$

where $\beta$ is the ratio $C_g/C_\Sigma$ ($C_\Sigma$ is the total capacitance of the Cooper pair island) $\hat{n}_c$ is the charge number operator and $V^0_{\text{rms}}$ is the root-mean-square

voltage of the resonator in its ground state. Here we assume the cavity and qubit decay rates $\kappa$ and $\gamma$ are much lower than the coupling rate $g_{01}$, i.e. $g_{01} \gg \gamma, \kappa$. This is called the strong coupling regime.

The qubit-resonator detuning is denoted as $\Delta_l = \omega_{l,l+1} - \omega_r$ where $\omega_{l,l+1} = \omega_{l+1} - \omega_l$ is the qubit transition frequency and $\omega_r$ the resonator frequency. The case when $|\Delta_0| \gg g_{01}$ and $|\Delta_0 + \alpha| \gg g_{01}$ is called the dispersive regime [34]. In this regime and by restricting ourselves to the ground and first excited state of the transmon we get an effective Hamiltonian [34]

$$\hat{H}_{\text{eff}} = \frac{\hbar\omega'_{ge}}{2}\hat{\sigma_z} + (\hbar\omega'_r + \hbar\chi\hat{\sigma_z})\hat{a}^\dagger\hat{a} \tag{2.27}$$

where the primes represent renormalized frequencies $\omega'_r = \omega_r - \chi_{12}/2$ and $\omega'_{01} = \omega_{01} + \chi_{01}$. Here

$$\chi = \chi_{ge} - \frac{\chi_{ef}}{2} \quad \text{and in general} \quad \chi_{l,l+1} = \frac{g^2_{l,l+1}}{\omega_{l,l+1} - \omega_r} \tag{2.28}$$

represent the resonator frequency shift due to the qubit state, for $|g\rangle$ it gets higher and for $|e\rangle$ it gets lower. From equation 2.28 one can interpret a shifts of the resonator frequency depending on the qubit state. That effect can be used to detect the state of the qubit. The Hamiltonian can also be rearranged to

$$\hat{H}_{\text{eff}} = \left(\frac{\hbar\omega'_{ge}}{2} + \hbar\chi\hat{a}^\dagger\hat{a}\right)\hat{\sigma_z} + \hbar\omega'_r\hat{a}^\dagger\hat{a}. \tag{2.29}$$

Now we can see that also the qubit frequency is shifted by $2\chi$ by each photon in the resonator. This is the dispersive ac-Stark shift.

## 2.5 Qubit manipulations

In order to manipulate the state of a qubit it must be subjected to an electric field in close vicinity to its transition frequency. In the dispersive limit this means the presence of an off-resonant photon in the resonator which has not been taken into consideration so far. It is however important to understand the effect of the drive amplitude and frequency on the qubit. In Ref. [16] we find the dispersive Jaynes-Cummings Hamiltonian 2.27 for a CPB combined with the off-resonant driving field at a frequency $\omega_d$, phase $\phi$ and an amplitude $\epsilon(t)$

$$\hat{H}_d(t) = \hbar\epsilon(t)(\hat{a}^\dagger e^{-i\omega_d t} + \hat{a}e^{i\omega_d t}) \tag{2.30}$$

yields the Hamiltonian

$$\hat{H} = \frac{\hbar}{2}[\omega_{ge} + 2\frac{g^2}{\Delta}(\hat{a}^\dagger\hat{a} + \frac{1}{2}) - \omega_d]\hat{\sigma}_z + \hbar\frac{g\epsilon(t)}{\Delta}\hat{\sigma}_x + \hbar(\omega_r - \omega_d)\hat{a}^\dagger\hat{a} + \hbar\epsilon(t)(\hat{a}^\dagger + \hat{a}). \tag{2.31}$$

The amplitude, phase and frequency of the external driving field is tunable in an experimental setup. We can thus choose a rotating reference frame by varying $\omega_d$. Driving at

$$\omega_d = \omega_{ge} + (2n+1)\frac{g^2}{\Delta} \tag{2.32}$$

equation 2.31 becomes

$$\hat{H} = \hbar\frac{g\epsilon(t)}{\Delta}\hat{\sigma}_x + \hbar(\omega_r - \omega_{ge} + (2n+1)\frac{g^2}{\Delta})\hat{a}^\dagger\hat{a} + \hbar\epsilon(t)(\hat{a}^\dagger + \hat{a}). \tag{2.33}$$

such that we rotate the Bloch vector around the x axis of the bloch sphere at the Rabi rate $\Omega = \frac{g\epsilon(t)}{\Delta}$ if the phase of pulse is $\phi = m\pi$(m is an integer). The azimuthal angle of the rotation axis can in general be tuned by the phase of the qubit drive.

## 2.6 Sideband transitions

The transitions on the joint system of a qubit and a resonator $|g0\rangle \leftrightarrow |e1\rangle$ and $|g1\rangle \leftrightarrow |e0\rangle$ are called blue and red sidebands respectively. They can be used to mediate interaction between multiple qubits in a controlled manner. A single photon sideband transition is forbidden in our circuit QED system [37] but a two photon transition is allowed. As depicted in Figure 8 the sideband transitions are then mediated via a quasi state which is detuned from the dispersively coupled $|ln\rangle$ states. Let us now focus on the blue sideband. We can drive the transition using two different tones $\omega_{d1}$ and $\omega_{d2}$ or a single tone where $\omega_{d1} = \omega_{d2} = \omega_d$. They must be chosen such that

$$\omega_{d1} + \omega_{d2} = \omega_{ge} + \omega_r \tag{2.34}$$

in the two tone case or $2\omega_d = \omega_{ge} + \omega_r$ with a single tone. Because this is a two photon transition the probability of it occurring is much lower than the single

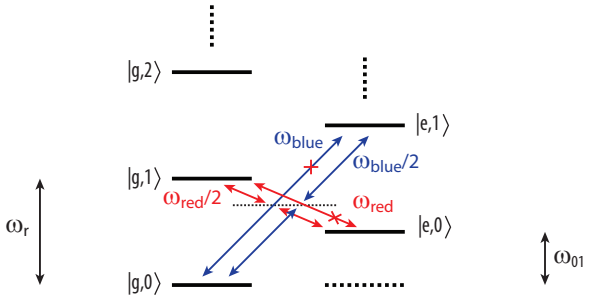


Figure 8: Operations on the joint qubit-resonator system is possible with two photons on the sidebands. In the case of a single tone, as shown here, the transition gets mediated via a quasi level midway between the qubit and the resonator levels.

photon on resonance transition only on a qubit. A single tone blue sideband on a resonator-transmon system has the Rabi rate

$$\Omega_{\mathrm{BSB}} = \frac{g\Omega^2}{4(\omega_{ge} - \omega_d)^2}\left(1 - \frac{\omega_{ge} - \omega_d}{\omega_{ef} - \omega_d}\right) \tag{2.35}$$

where $\Omega$ is the Rabi rate when driving the qubit on resonance with the same amplitude. Here we have have added a correction term from the derivation in Ref. [37] for a Cooper pair box which accounts for the lower anharmonicity of the transmon qubit[2].

## 2.7 CNOT and controlled-Z gates

It has been shown [35] that a single qubit and a two qubit logic gate, called a controlled NOT (CNOT) gate, can be used to implement an arbitrary unitary operation on multiple qubits forming a universal set of logic gates. Its function is to flip a target qubit, T, depending on a control qubit, C. In the basis $|gg\rangle, |ge\rangle, |eg\rangle, |ee\rangle$ (notation: e.g. $|gg\rangle = |g\rangle_{\mathrm{C}} \otimes |g\rangle_{\mathrm{T}}$) we can represent the gate as

$$U_{\mathrm{CNOT}} = \begin{pmatrix} 1 & 0 & 0 & 0 \\ 0 & 1 & 0 & 0 \\ 0 & 0 & 0 & 1 \\ 0 & 0 & 1 & 0 \end{pmatrix}. \tag{2.36}$$

Closely related to the CNOT gate is the controlled-Z gate. It applies a $\pi$ phase on the target qubit depending on the control qubit. By using the same basis as before we can represent the controlled-Z gate as

$$U_{\mathrm{CZ}} = \begin{pmatrix} 1 & 0 & 0 & 0 \\ 0 & 1 & 0 & 0 \\ 0 & 0 & 1 & 0 \\ 0 & 0 & 0 & -1 \end{pmatrix}. \tag{2.37}$$

One can obtain a CNOT gate by applying a Hadamard gate, $\mathbb{H} = \begin{pmatrix} 1 & 1 \\ 1 & -1 \end{pmatrix}$, on the target qubit on both sides of a controlled-Z gate

$$U_{\mathrm{CNOT}} = (\mathbb{1} \otimes \mathbb{H}) U_{\mathrm{CZ}} (\mathbb{1} \otimes \mathbb{H}). \tag{2.38}$$

# 3 Experiments

The experiments we performed consist of three parts; developing a high Q 3D cavity, characterization of a single qubit in a 3D cavity and characterization and operations on two qubits in a 3D cavity. First we will however introduce the setup and some of the technical sides of the experiment.

[2] adaptation from [37] via internal communication and private notes of Peter Leek.

## 3.1 Setup

A circuit diagram of the main experimental setup is shown in Figure 9 and we will discuss it in three sections. First we talk about how to cool our sample down in a dilution refrigerator, then we will talk about the electrical cabling inside the fridge and finally a short discussion about the microwave equipment outside the generator.

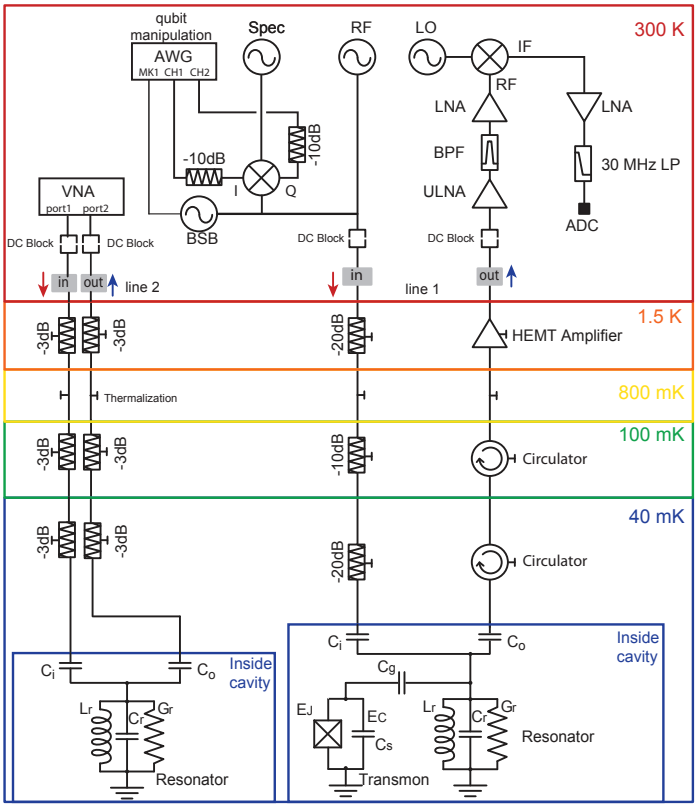


Figure 9: A circuit diagram of the measurement setup which has been installed for 3D circuit QED experiments. We use a cryogenic dilution refrigerator which a base temperature of 40 mK. The setup has two slots denoted line 1 and line 2. Line 1 is designed for low photon numbers as is desired in qubit experiments. Line 2 is designed for high photon numbers which gives a stronger signal in cavity transmission experiments. Out side the fridge at 300 K we have various microwave equipment which is described in 3.1.3. The Figure is adapted from [28].

### 3.1.1 Dilution refrigerator

Our qubits are based on superconducting circuits and must thus cool below the critical temperature of the material, which in our case is Al with $T_c = 1.2$ K. Furthermore we require the qubit to be cooled to its ground state such that $\hbar\omega_{ge} \gg k_{\mathrm{B}}T$. The method used to get to the mK temperatures is a closed pumping cycle is described below. This cycle however requires an environment at temperatures around 1.5 K or below. The two methods used to create such an environment divides dilution refrigerators into two categories, either with or without cryogenic liquids. Cryogenic dilution refrigerators are the traditional design and use a liquid helium bath and evaporative cooling to create a thermal reservoir at 1.5 K. A more modern technology is used in cryogen-free dilution refrigerators where helium is pumped through membrane in a closed cycle creating a cooling effect [38]. This design has the convenience of not having to maintain a liquid helium bath with frequent refills.

To cool our sample to temperatures around 40 mK we use a cryogenic dilution refrigerator. The process is based on the circulation of a $He^3/He^4$ mixture. It has two phases below the He triple point, a $He^3$ rich phase and a $He^4$ rich phase. As the $He^3$ is pumped through $He^4$, the phase separation is distorted. In order to regain equilibrium thermal energy is extracted from the environment creating a cooling effect.

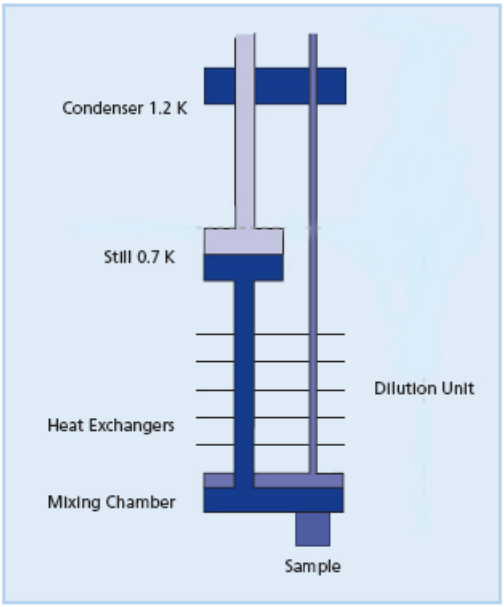


Figure 10: The pumping cycle of $He^3/He^4$ mixture in a dilution refrigerator. When $He^3$ is pumped through $He^4$ the phase separation is distorted. To counter this distortion energy is taken from the environment which gets colder. (Picture taken from Oxford Instruments website).

The cycle is shown in Figure 10 were the dilution process takes place in the mixing chamber. $He^3$ is pumped from there into the still where it evaporates. The still has a big circumference and is slightly heated to facilitate the process. The evaporated $He^3$ is pumped out of the fridge. At room temperature, on the other side of the pump, the $He^3$ is pressed through cold traps and into the fridge to a condenser. There it precooled in the 1K pot and the returning $He^3$ cool it via heat exchangers back to a condensed state.

### 3.1.2 Cabling

Our setup has two experimental slots, lines 1 and 2, as seen in Figure 9. Connecting a cavity at 40 mK inside a dilution refrigerator to microwave equipment at room temperature requires specific cabling techniques.

The cavity is connected to semi-rigid UT-85 cables that feed the microwave signal in and out through the top of the fridge, see Figure 11 a. We use coaxial cables made of copper from base to the 100 mK stage, stainless steel from 100 mK to 1.5 K and cables made of a copper inner conductor with a stainless steel outer conductor from 1.5 K to 300 K. Here one must choose between the high thermal conductance of copper and the high electrical conductance of stainless steel. We connectorize the cables with SMA connectors. This must be done carefully in order to minimize reflection. Losses in the cable transmission increase with frequency. The transmitted power though line 2 is shown in Figure 11 b where the input line is connected to the output line with a through at room temperature.

The cables provide a connection to equipment at room temperature. Cooling measures must be taken to cool both the inner and outer conductor as well as minimize thermal noise. We put attenuators at every temperature stages to thermally connect the inner and the outer conductor of the cable. A copper bulk and solder braids are then used to thermally anchor the attenuator to the

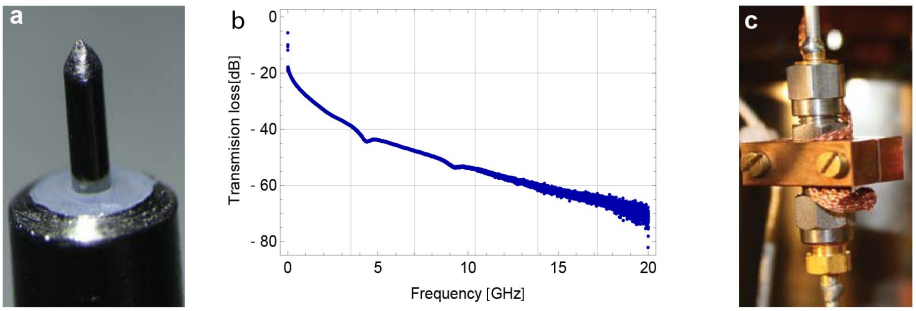


Figure 11: a) A stripped semi-rigid UT-85 cable as used inside the dilution refrigerator. b)The loss in the cables through line 2 of the setup when a cavity is replaced by a through, see Figure 9. The two dips at 4 and 9 GHz suggest resonance due to impedance mismatch in one of the cables or in the through. c) Solder brades wraped around an attenuator and fastened by a copper block.

stage (see Figure 11 c) allowing heat to dissipate before reaching the cavity.

On line 2 we put only -18dB(6x3dB) attenuation as it is intended for high photon number experiments. That is sufficient for cavity experiments(without a qubit). Line 1, however, is used for qubit experiments and requires -50 dBm attenuation on the input line to dampen thermal noise in addition to thermalizing the cable. Due to this high input attenuation amplification is needed at the output line. A HEMT amplifier is located at the 1.5 K stage amplifying the signal by about 30 to 40dB [28]. In addition to amplifying the output signal it also thermally anchors the cable. The output line has circulators at the mixing chamber and 100 mK stage to attenuate radiation coming from the amplifier and thermalize the cable.

### 3.1.3 Microwave equipment

Outside of the fridge we have the various electrical components needed for the experiment. We use microwave generators, *Agilent technologies E8257D, Rohde&Schwarz SMF 100A* synchronized by a Rubidium clock *SRS model FS725 Rubidium frequency standard* to measure and manipulate our sample. The microwave pulses are gated with an arbitrary wave generator (AWG) *Tekrionix AWG5014* either by on/off marker triggering of the generators or by frequency mixing on an upconversion board as described in Ref. [39]. One can in both cases control the amplitude of the pulse but only in the frequency mixing gives phase control. The output signal from the fridge is both amplified with low noise amplifiers (LNA) and filtered with a band pass filter (BPF) and a low-pass filter (LPF) on a downconversion board. We then digitize the data using an Aquiris data acquisition card. Both the downconversion board and the upconversion board were made by Marek Pechal.

## 3.2 Sample fabrication: 3D cavity and qubit

The inspiration for this thesis is the improvement in lifetimes observed in high-Q 3D cavities [1]. Before making our own cavity we did simulations of a realistic design. The simulations gave information about the electric field inside the cavity, its resonance frequency and the design of the coupling pins. We proceeded to making our design out of various alloys and metals. Having not reached the same Q factors as in Ref. [1] in our usual setup we put our cavity in another setup which has the obvious difference of a magnetic shield. In that setup we achieved an internal Q factor of two million.

### 3.2.1 3D cavity simulations

We used Comsol Multiphysics 4.2 to simulate the $E_z$ distribution in the cavity with dimensions 32 x 15.5 x 5mm$^3$. This model includes a sapphire chip, which is the qubit substrate and coaxial coupling pins. The pins require finer meshing because to they have small features compared to the rest of the cavity and the excitation of the field is there. The excitation frequency at the pins can

be swept. In Figure 12 we see the $E_z$ distribution at the (1,1,0) resonance frequency. The field concentrated at the middle of the x-y plane of the cavity but independent of the z coordinate. In addition simulated the transmission from one coaxial coupling port to the other. With the chosen dimensions we get a transmission spectrum around the first mode at 10.799 GHz. We fit the peak with a Lorentzian function (Eqn. 2.7) as seen in Figure 13 a. This frequency is well suited for dispersive coupling to qubits at 4-9 GHz. By simulating with very high conductivity in the walls of the cavity, $\approx 10^{30}$ S, we assume no internal losses i.e. $Q_{\text{int}} = \infty$. From this simulated transmission we can then calculate the expected $Q_{\text{ext}} = Q_L$ from the equations given in section 2.1.2. Changing the the pin lengths we can vary $Q_{\text{ext}}$ as shown in Figure 13 b.

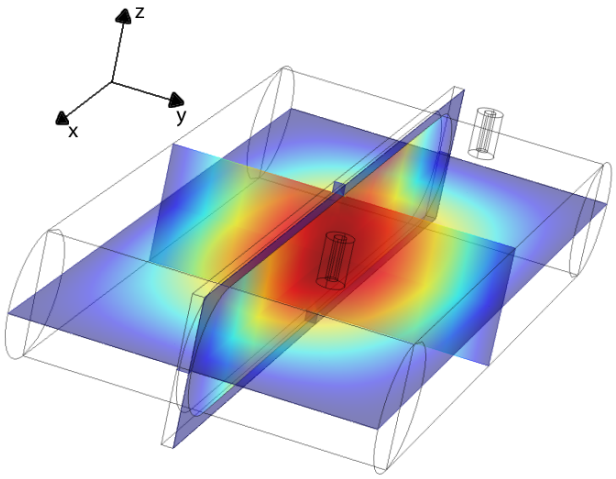


Figure 12: The simulated cavity. We see a color coded $E_z$ distribution in tree planes at the (1,1,0) resonance frequency. This design includes a sapphire chip perpendicular to the y axis and coupling ports to couple microwave signals in and out of the cavity.

The resonance frequency of the (1,1,0) mode according to Equation 2.2 is 10.742 GHz in comparison to 10.799 GHz from the fit in Figure 13 a. In Figure 13 b we have added measured values (Red dotts) for -0.3 mm and 0.2 mm from warm measurements on the first mode. This corresponds relatively well to the simulation.

### 3.2.2 Physical realization with various materials and shielding

We had a cavity made with inner dimensions of 32 x 15.5 x 5 mm$^3$ as in the simulation and 47 x 20 x 15 mm$^3$ outer dimensions (see Figure 14 a). The pins used couple to the cavity are made out of copper with a gold coating.

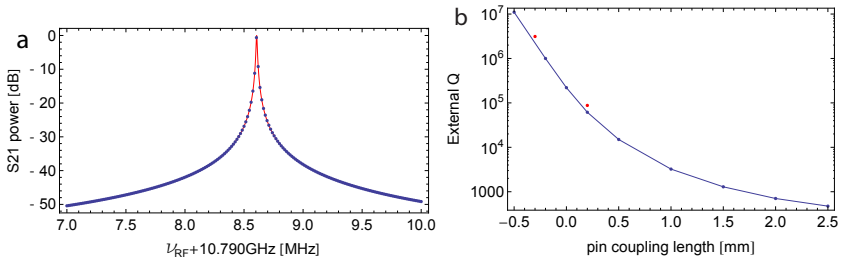


Figure 13: a) The simulated transmission of the cavity at the (1,1,0) mode. b) $Q_{\text{ext}}$ of the (1,1,0) mode depends strongly on the pin length as shown. The length is measured relative to the wall on the cavity. Negative pin length means that the pin does not extend out of the pin hole.

Their length is adjusted by filing them down, there by tuning $Q_{\text{ext}}$. We want $Q_{\text{ext}} \geq Q_{\text{int}}$ in reference to the expected value of $Q_{\text{int}}$ in order for the measured $Q_L$ to be more sensitive to $Q_{\text{int}}$ than $Q_{\text{ext}}$ (see Eqn. 2.6). I our case we expect an internal Q of about one million. This is corresponds to filing the pins to a length of about -0.2 mm relative to the cavity wall.

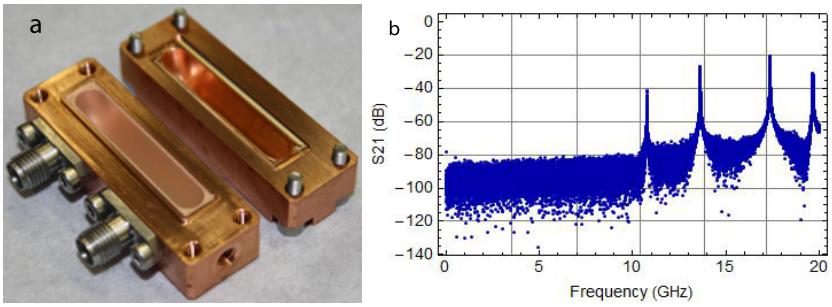


Figure 14: a) The 3D cavity design with coupling pins mounted. The left half has a slit for stable insertion of a chip with a qubit. b) The measured spectrum of the cavity at room temperature. The free spectral range is about 3-4 GHz for the first 3 modes.

We measured $Q_{\text{int}}$ for various Al alloys, Cu and Cu coated with a 0.5 $\mu$ thick layer of pure aluminum both at room temperature and at 40 mK. The various Al alloys vary mainly in the amount of Si and Mg in them. Al ac-hard and Al warm-hard vary by hardening temperatures. The results can be seen in Table 1. When measuring at room temperature we can calibrate the vector network analyzer (VNA) for losses in the cables connecting to the cavity. When measuring at 40 mK we correct for losses in the fridge cables by measuring it separately warm, see Figure 11, and subtracting it in the data processing.

At room temperature (R.T.) we observe, as expected, a higher $Q_{\text{int}}$ of Cu than of Al because it has higher electric conductivity. At 40 mK the Cu cavity

reaches $Q_{\text{int}} = 15000$ while the Al cavities enter a superconducting phase and reach up to about $Q_{\text{int}} = 100000$. The transmission spectrum is measured with

| Alloy | Cu | Al/Cu | Al6061 | Al ac-hard | Al Plan | Al warm-hard |
|---|---|---|---|---|---|---|
| $\nu_{\text{r}}$@ R.T. [GHz] | 10.716 | 10.765 | 10.860 | 10.692 | 10.889 | 10.850 |
| $Q_{\text{int}}$@ R.T. | 4597 | 3451 | 3435 | 1903 | 2450 | 2419 |
| $Q_{\text{int}}$@ 40 mK | 15378 | 71895 | 94819 | 109614 | 71162 | 54220 |

Table 1: The table shows $\nu_{\text{r}}$, the resonance frequency of the (1,1,0) cavities mode measured at room temperature and $Q_{\text{int}}$ both at room temperature and 40 mK with no magnetic shielding.

a VNA at room temperature. Fitting the 1. mode with a Lorentzian we retrieve the frequencies in Table 1. The fit also gives us $Q_L$ and the insertion loss $Il$ such that we can calculate $Q_{\text{int}}$ from Equation 2.8. The Q factors at 40 mK are measured in the same way but the loss in the fridge cables must be accounted for in order to get the correct insertion loss.

Higher Q factors have been observed [1]. We thus put a Al6061 cavity in another fridge which has magnetic shielding. This gave $Q_L$ of one million from the transmission spectroscopy shown in Figure 15. Assuming the same $Q_{\text{ext}}$ as measured at room temperatures we get a $Q_{\text{int}}$ of two million. Figure 16 a shows a linear dependence between the spectroscopy power and the peak height as expected for a harmonic oscillator and no other decay channels affect the transmission. The power applied at the cavity input port is estimated roughly from the generator output power and the expected attenuation in the cables. The power of a resonant photon in the cavity can be estimated by the photon energy $\hbar\omega_{\text{r}}$ and the cavity decay rate $\kappa$, $P_{\text{photon}} = \hbar\omega_{\text{r}}\kappa$. By applying a power $P_{\text{in}}$ at the input port at the frequency $\omega_{\text{r}}/2\pi$ on can estimate the number of resonant as $n = P_{\text{in}}/P_{\text{photon}}$. We also see in Figure 16 b that the internal Q does not depend on the applied power.

### 3.2.3 The qubit

One of the differences between a transmission line resonator and a 3D cavity resonator is that the mode volume is much larger in the 3D case. This means that the electric field strength per unit energy, $E$, is lower than in the 2D case. In order to maintain the same coupling strength, $\hbar g = Ed$, a bigger dipole moment, $d$, of the qubit is needed.

The qubit fabrication was done by Dr. Johannes Fink using electron-beam lithography and evaporative deposition onto a sapphire substrate. They consisted of two 250 x 500 $\mu m^2$ aluminum islands, see Figure 17. The islands are 100 - 200 $\mu m$ apart but connected with a 1 $\mu m$ wide wire with a Josephson junction in the middle.

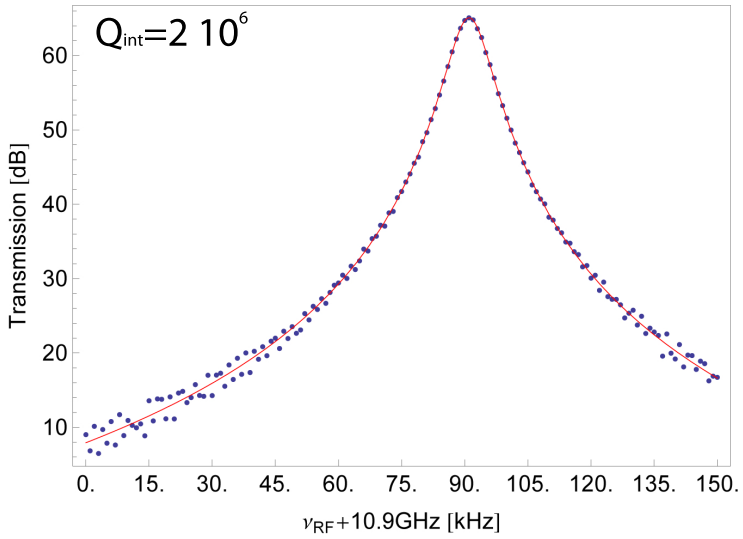


Figure 15: Transmission spectroscopy of first cavity mode in a dilution refrigerator with magnetic shielding. The internal Q calculated from this measurement is two million, indicating the importance of magnetic shielding.

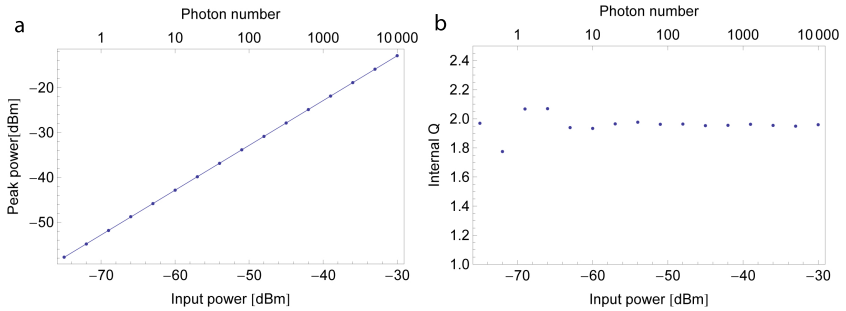


Figure 16: a)The peak of the Lorentzian scales linearly with the applied power at its input port. b) We observe that $Q_{\text{int}}$ is independent of the applied power.

## 3.3 Measurement techniques and single qubit characterization

We characterized 4 qubits and labeled them: qubit 1, qubit 2, qubit 3A and qubit 3B. This section describes the characterization experiments performed on the qubits and the resonator. We begin by discussing the transmission trough a cavity with a qubit around the lowest resonance frequency (1,1,0) at various powers. Then we describe how the state of the qubit can be read out from the transmission signal and how to perform both continuous and pulsed qubit spectroscopy using low readout powers. We then talk about qubit readout

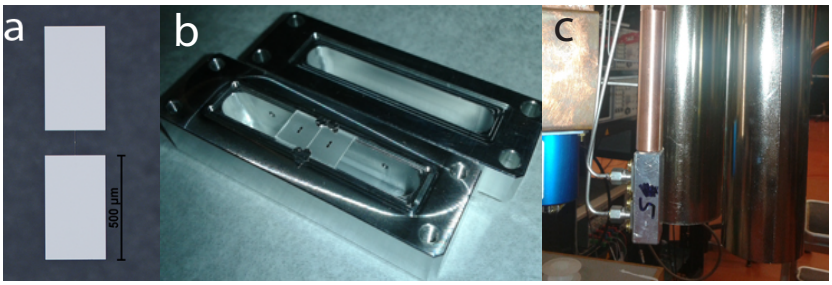


Figure 17: a)A picture of the qubit taken with an optical microscope. The Josephson junction is in the middle of the wire between the two islands. b) Two qubits on separate chips mounted in a 3D cavity. c) A 3D cavity mounted in a dilution refrigerator.

with high powers. From there we proceed to discuss Rabi, Energy relaxation time, and Ramsey experiments used to calibrate qubit manipulation pulses and measure the lifetimes and frequency of the qubit. Thereafter we discuss both single and two tone blue sideband transitions on the joint qubit-resonator system before introducing state tomography and performing it on a single qubit. Finally we state and discuss the parameters of our qubits.

### 3.3.1 Resonator spectroscopy

With a qubit inside a cavity, mounted and cooled down in a fridge we measure the transmission through the cavity. According to the Hamiltonian in Eqn. 2.27 the resonator frequency shifts in the presence of a qubit even if it is in the ground state. Figure 18 a shows the resonator transmission spectrum as a function of the input power when the qubit is not excited. With the system in its ground state we see a peak at 9.058 GHz. As the power is increased the transmission spectrum ceases to follow a Lorentzian shape. At high powers a peak reappears at the bare resonator frequency at 9 GHz, see Figure 18 b. This resembles a classical cavity where the photon numbers are large enough to mask the qubit induced non-linearity of the circuit [40, 41, 42]. The shape is not perfectly Lorentzian so it is unreliable to get a reasonable $Q_L$ with this measurement. A fit can still be made to get a rough estimate. Generally the measured Q of the bare cavity is lowered when a qubit in put into the cavity. The cavity used in Figure 18 is made out of Al6061. Without the qubit the internal Q factor is $Q_{\text{int}} = 94819$ at 40 mK but has been lowered to $Q_{\text{int}} = 21595$ with a qubit in the cavity.

### 3.3.2 Qubit readout and spectroscopy

To illustrate the qubit readout we measured the resonator response around the cavity resonance both for the qubit in the ground state, see Figure 19 a and in

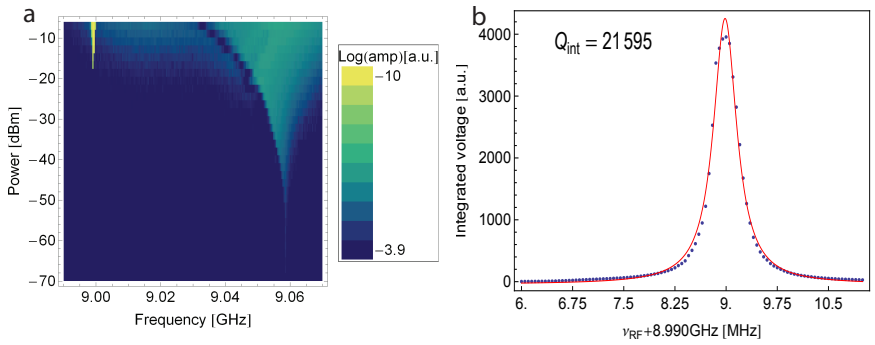


Figure 18: a) Resonator transmission spectrum. At low powers we observe a shift of the resonance frequency as predicted by the Jaynes-Cummmings hamiltonian. At high powers a peak appears at the bare reonator frequency.

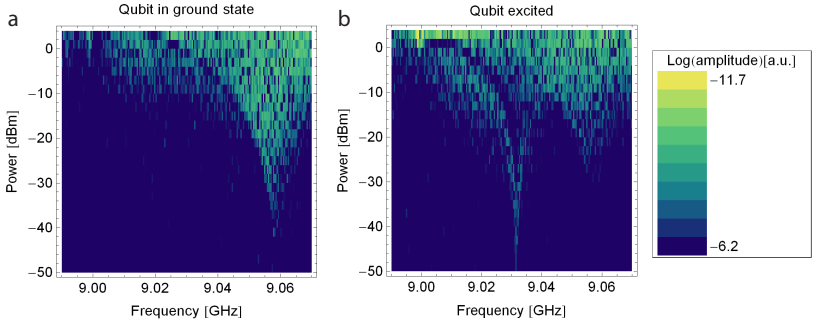


Figure 19: Transmission spectroscopy around the first mode (1,1,0) of the cavity for varying power. The qubit is in the ground state in a) and in the first excited state in b). The qubit state can be determined by the frequency shift at low powers or by the transmitted power at the bare resonance frequency when high power is applied.

the excited state, see Figure 19 b[1]. At low powers($\sim$ 40 dBm) we see a qubit state dependence of the resonance frequency as described in Equation 2.27. At high powers the transmitted signal at the bare resonance frequency is qubit state dependent. This can be used to readout the qubit state as described in Ref. [40] with a higher signal-to-noise ratio than in the low power regime. Having now described the qubit-state dependent cavity responses we proceed to explain the measurement methods.

To find the qubit frequency we apply a tone, called the RF, at the ground state resonance frequency in the low power regime and sweeping another spectroscopy tone with high power. When the spectroscopy tone coincides with the

[1]Note that for Figure 19 b we had calibrated our pulses to excite the qubit.

qubit excitation frequency the qubit will be driven from the ground state. We choose the low power regime to initially determine the qubit transition frequency because the required readout power easier to estimate than in the high power case. Because the shift of the resonator frequency at low powers is qubit state dependent the transmitted RF signal will decrease. Figure 20 shows this type of spectrum.

The multiple resonances in Figure 20 a are due to the ac Stark shift[43], also called number splitting [44], i.e. the lowering of the qubit transition frequency for each number of photon in the resonator, see equation 2.29. The frequency between adjacent resonances is $2\chi$. By lowering the readout power one observes the that the lower frequencies resonances, which correspond to higher photon numbers, diminish. The single resonance in Figure 20 a is from a time resolved measurement i.e. if we separate the spectroscopy tone and the RF tone in time into two subsequent pulses (see Figure 21 b) the resonator will be empty when the qubit transition is driven.

Having found the qubit transition frequency we proceed to the high power readout(HPR). The qubit state is first prepared and the read out with a pulse at the bare resonance frequency and various powers. Before the pulses have been calibrated (see Section 3.3.3 and 3.3.5) the state is prepared in the ground state by applying no pulse at all or by applying a pulse at an arbitrary amplitude and length at the qubit transition frequency such that the qubit is partially excited. The three traces in Figure 21 b are the resonator responses integrated over the first 50 $\mu$s after preparing the g, e and f states of the qubit. Here the preparation pulses have been calibrated for controlled population of the g, e and f states. By choosing the readout power which has a the greatest state dependent response difference we can achieve high signal-to-noise enabling single shot readout of the qubit state.

A feature of the HPR is that the readout pulse highly populates the cavity. For many experiments one must wait until all the photons have decayed and the cavity is empty before triggering another pulse sequence. In cases when the pulse sequences are much shorter than the time needed to empty the cavity the

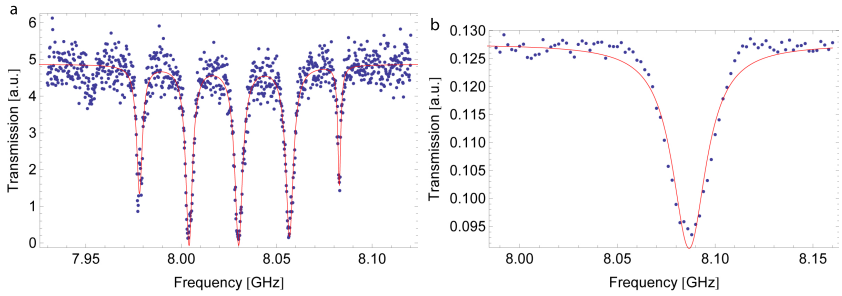


Figure 20: The qubit frequency is found by spectroscopy such that the qubit excitation changes the resonance of the cavity.

HPR induces an overhead. In the samples used in this thesis the pulse sequences were up to $\sim 60$ $\mu$s long but the trigger interval required to empty the cavity was 2 ms.

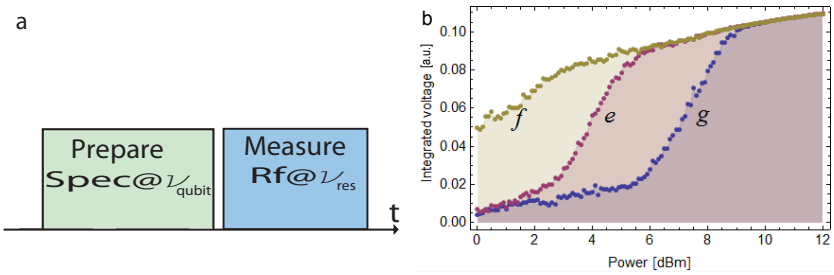


Figure 21: a) A pulsed measurement sequence. By pulsing the measurement we can prepare the qubit state without the effect of resonant photons in the cavity. b) The resonator response at the bare resonator frequency $\nu_B$ when the RF power is swept. The three traces represent represent different qubit state preparations before measuring; g is blue, e is red and f is yellow. This can be used for readout with a high signal-to-noise ratio.

### 3.3.3 Rabi oscillations

The measurement techniques discussed so far consist of a continuous measurement signal or pulses with arbitrary length and amplitude. For qubit manipulations it is however desirable to have precisely controlled pulse sequences. The pulse sequence for a Rabi experiment is shown in Figure 22.

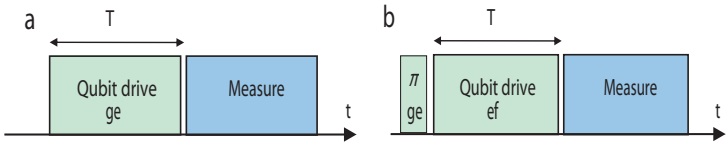


Figure 22: Pulse sequence for Rabi oscillation between the (a) $|g\rangle$ and $|e\rangle$ states and the (b) $|e\rangle$ and $|f\rangle$ states.

Referring to the Bloch vector rotation in Section 2.3 we want to calibrate for a $\pi$ pulse. This is done with a Rabi experiment. Applying a pulse at qubit transition frequency we start to rotate the state around a horizontal axis on the Bloch sphere and the total rotation is determined by the integral of the Rabi rate $\Omega$ over the duration of the pulse. As $\Omega$ depends on the drive pulse amplitude we can determine a $\pi$ pulse in two ways: By having a fixed amplitude and varying the pulse length or vice versa. We can monitor the vertical component of the state by projective measurements. By exciting the qubit first to the e-state one can do a Rabi experiment on the e-f transition. In Figure 23 we see Rabi

oscillations between the (a) $|g\rangle$ and $|e\rangle$ states and the (b) $|e\rangle$ and $|f\rangle$ states where the pulse length is varied and the amplitude is fixed. A fit to the data yields a $\pi$ pulse of 19.7 ns for the g-e transition and 29.7 ns for the e-f transition.

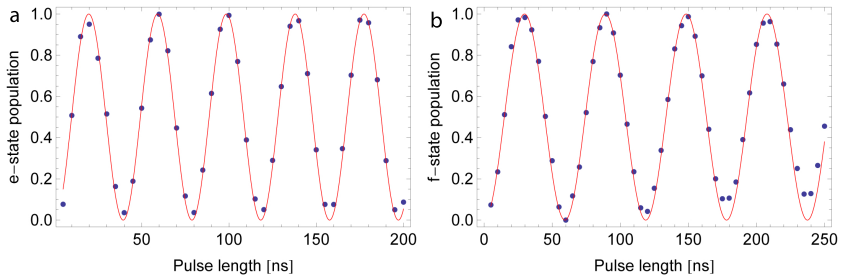


Figure 23: Rabi oscillation between a) the $|g\rangle$ and $|e\rangle$ states and b) the $|e\rangle$ and $|f\rangle$ states. At a fixed driving power the Bloch vector is rotated about a horizontal axis and we see its z component oscillate.

### 3.3.4 Energy relaxation time measurements

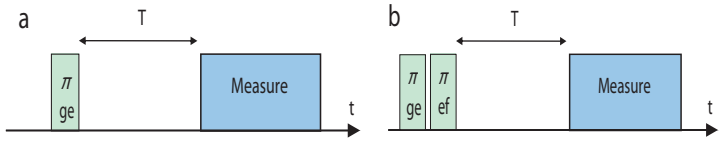


Figure 24: Pulse sequence for an energy relaxation time, $T_1$, measurement on (a) the $|e\rangle$ state and (b) the $|f\rangle$ state.

The energy relaxation time determines the rate at which the qubit decays from its excited state. By exciting the qubit with a $\pi$ pulse and varying the waiting time T before reading out the state (see Figure 24) we observe an exponential decay as seen in Figure 25. To excite qubit to the $|f\rangle$ state it is first excited to the $|e\rangle$ state in the scheme in Figure 24 b. By fitting $\mathrm{p} = \exp\left(\frac{-\mathrm{T}}{T_1}\right)$ to the data we extract an energy relaxation time $T_1 = 14.7$ $\mu$s for the $|e\rangle$ state and $T_1 = 11.3$ $\mu$s for the $|f\rangle$ state.

### 3.3.5 Ramsey oscillations

The qubit transition frequency can be determined with more precision using Ramsey oscillation than spectroscopy. Form equation 2.32 we see that the detuning of the drive frequency $\nu_\mathrm{d} = \omega_\mathrm{d}/2\pi$ from the qubit transition frequency $\nu_\mathrm{ge} = \omega_\mathrm{ge}/2\pi$ leads to a rotation around the z axis of the Bloch sphere at a frequency $\nu_\delta = |\nu_\mathrm{d} - \nu_\mathrm{ge}|$. We apply a slightly detuned $\pi/2$ pulse, wait for a

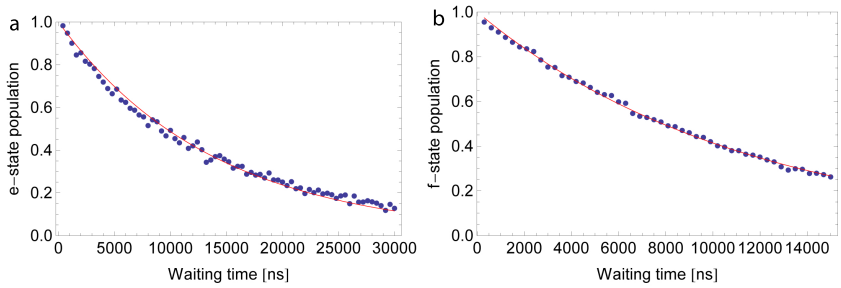


Figure 25: T1 measurement. By exciting the qubit and varying the waiting time before measuring the state we can determine the energy relaxation time of the qubit

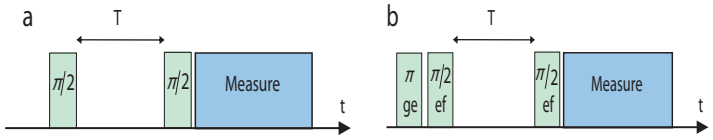


Figure 26: Pulse sequence for a Ramsey experiment on (a) the g-e transition and (b) the e-f transition. Two $\pi/2$ pulses, separated by a varying time T, are applied slightly off-resonant from the qubit transition frequency.

time T and do another $\pi/2$ pulse around the same axis, see Figure 26. During the time T the qubit acquires a phase $\phi_{\mathrm{q}} = T\nu_\delta$ such that by varying T we observe oscillations at a frequency $\nu_\delta$ between the two states involved in the experiment, either $|g\rangle$ and $|e\rangle$ or $|e\rangle$ and $|f\rangle$. $\nu_\delta$ is then used to determine $\nu_{ge} = \nu_{drive} \pm \nu_\delta$(+ or- depends on the detuning we choose). A measurement of the Ramsey oscillations is shown in Figure 27. The oscillations are damped due to qubit dephasing such that the population of the higher state is given as

$$\mathrm{p} = \frac{1}{2}(1 + \cos(\nu_\delta \mathrm{T}) exp(\frac{-\mathrm{T}}{T_2})), \tag{3.1}$$

where $T_2$ is the qubit dephasing time. The maximum dephasing time is $T_2 = 2T_1$. From fits to the data in Figure 27 a we obtain $\nu_\delta = 0.48$ MHz and $T_2 = 9.1$ $\mu$s and from Figure 27 b $\nu_\delta = 3.23$ MHz and $T_2 = 2.6$ $\mu$s

### 3.3.6 Blue sideband transitions

Blue sidebands transitions (BSB) are observed with spectroscopy, see Figure 28. We see from Figure 28 that the BSB frequency is lowered as the drive power is increased. This effect is an ac-Stark shift from the strong drive tone which we will note as $\chi_{\mathrm{d}}$ and was observed by Wallraff et al. [21]. Experiments which vary the drive power thus become more involved as the BSB frequency shifts.

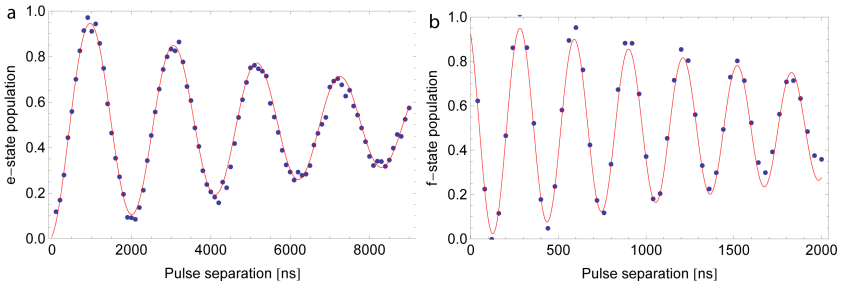


Figure 27: Ramsey oscillation. The frequency of the oscillations is the detuning of the drive from the qubit transition frequency. The amplitude decay gives the dephasing time $T_2$.

As in the single qubit transitions we perform a Rabi experiment on the BSB. Figure 28 shows blue sideband Rabi oscillations. As the pulses get longer the

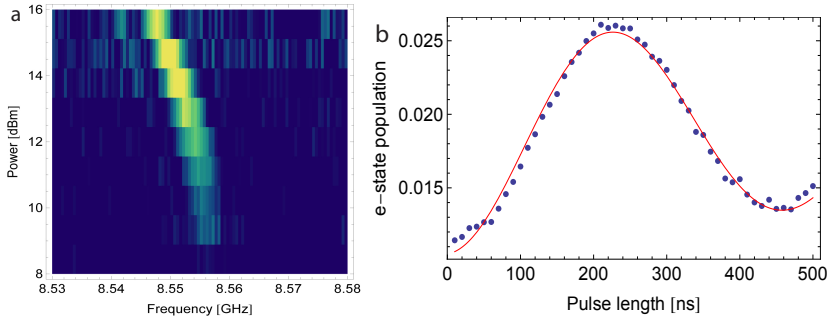


Figure 28: a) Blue sideband spectroscopy at various drive powers. The resonance shifts to lower frequencies with higher drive power due to an ac-Stark shift. b) Rabi oscillations be driven on BSB transition. The damping of the oscillations is because of the decay of the photon in the cavity.

oscillations are dampened. This is because of the photon decay in the resonator leading to a saturation in the excited state. We can however not quantify the $|e\rangle$ state population in a reasonable manner because the resonator photon also affects the readout signal.

We calculate the BSB Rabi rate for qubit 3A with Equation 2.35. The qubit is detuned from the resonator by $\Delta = 2.5$ GHz, with anharmonicity $\alpha = -372$ MHz and coupling constant $g = 192$ MHz. We drive it at powers which correspond to a Rabi frequency $\Omega = 12.665$ MHz. These parameters give a BSB Rabi rate $\Omega_{\text{BSB}} = 1.13$ MHz. We also drive the transition at the ac-Stark shifted resonance and measure a BSB Rabi rate $\Omega_{\text{BSB}} = 1.42$ MHz.

Ramsey oscillations are not as ease to perform on the BSB transition as in the single photon case. Driving the $\pi/2$ pulses in the Ramsey experiment on-resonance we are in a shifted rotating frame corresponding to the ac-Stark

shift. During the waiting period T, the system is no longer in the shifted frame creating an undetermined detuning. To determine the transition frequency more precisely we do Rabi oscillations for various frequencies. The resonant BSB frequency is then the one with the lowest Rabi frequency. Figure 29 a shows Rabi oscillations for various drive frequencies. In Figure 29 b we plot the Rabi rates versus the drive frequency yielding a resonance at 7.757 GHz.

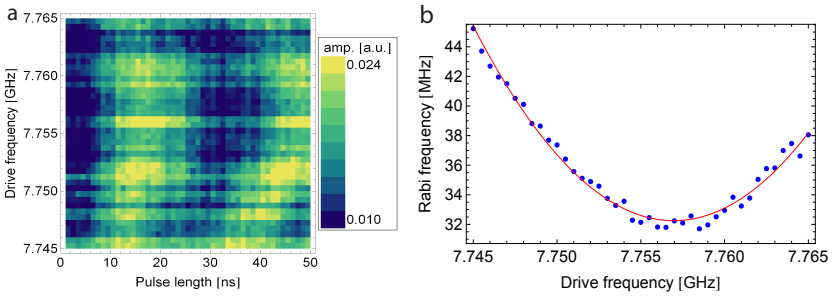


Figure 29: a) A 2D plot of a BSB Rabi oscillations at varying drive frequencies. b) BSB Rabi frequencies at varying drive frequencies. The Rabi frequencies increase with the detuning from the resonance of the transition such that the minimum yield the resonant drive frequency.

We have so far only discussed single tone sideband transitions where the two photons in the transition have the same frequency. It is also possible to do two tone blue sideband transition where the photons have different frequencies which add up to the required energy. Figure 30 shows a two tone spectroscopy. We observe a resonance at the where the two tones add up to 14.6757 GHz.

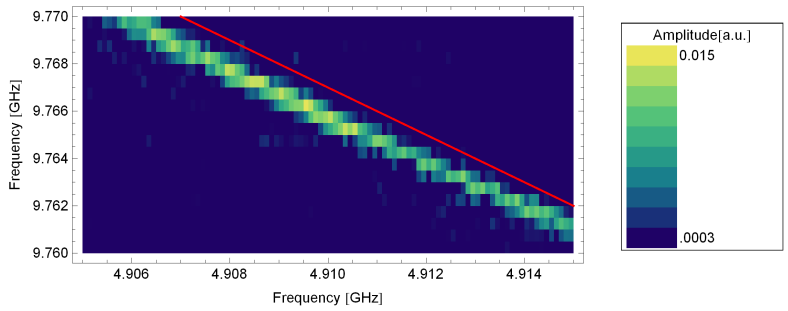


Figure 30: Two tone BSB spectroscopy. The resonance forms a line parallel to and about 1.7 MHz lower than the red line which represent the calculated resonance from Eqn. 2.34.

This resonance is about 1.7 MHz lower than the calculated value according

using Equation 2.34 which is drawn as a red line. The ac-Stark shift was not measured for in this case such that its effects are unknown.

### 3.3.7 State tomography

All measurements performed are projective i.e. the state is projected onto an axis on the bloch sphere. Not all the information about the state is retrieved in that way by a single measurement. To fully know the state of the qubit we must construct its density matrix. This is done with state tomography. Taking 4 different but identically prepared versions the state and applying the identity and the three Pauli operators on it before measuring one can reconstruct the Bloch vector and then use equation 2.20 to retrieve the density matrix. This is implemented as follows: The qubit state is prepared four times. After each preparation a different rotation corresponding to one of the operators $\mathbb{1}, \hat{\sigma}_x, \hat{\sigma}_y, \hat{\sigma}_z$ is applied and the state is measured. A total of 4 measurements. For 2 qubit state tomography the measurement operator is the defined as $\hat{M} = \sum_{i,j} \beta_{i,j} \hat{\sigma}_{j_A} \otimes \hat{\sigma}_{i_B}$.One must project the prepared state onto all combinations of the four operators used in the single qubit case, a total of 16 measurements.

When a density matrix $\rho$ has been measured one is often interested in comparing it with the theoretical matrix $\sigma$ corresponding to the same preparation. This can be done with a measure called fidelity

$$F^1(\rho, \sigma) = tr(\sqrt{\rho^{1/2} \sigma \rho^{1/2}}). \tag{3.2}$$

We also use another definition which does not require one to find the square root of a matrix.

$$F^2(\rho, \sigma) = tr(\rho \cdot \sigma). \tag{3.3}$$

Figure 31 shows state tomography where the state $|+\rangle = \frac{1}{\sqrt{2}}(|g\rangle + |e\rangle)$ has been prepared with a fidelity $F^1 = 0.987$.

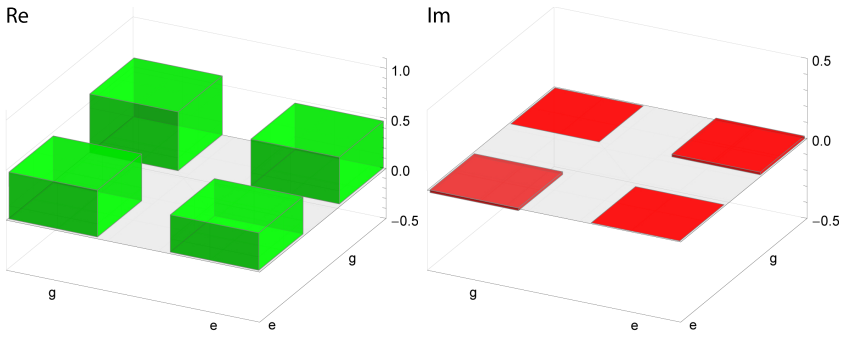


Figure 31: The reconstruction of the $|+\rangle\langle+|$ density matrix using state tomography with a fidelity of $F^1 = 0.987$.

### 3.3.8 Results

We characterized 4 qubits, two of which were on the same chip and were used for two qubit experiments. The qubits have about ten times longer lifetimes than in the typical charge qubits in a 2D architecture [25]. We note that $T1_{ef}$ is remarkably long and even longer than $T1_{ge}$ in some cases. This is surprising because the $|f\rangle$ state has more decay channels than the $|e\rangle$ and remains to be investigated.

The values of $E_J$, $E_C$ and $g$ are determined by inputting them as parameters the Hamiltonian in Equation 2.25 and numerically calculating the energy levels. We then tune $E_J$, $E_C$ and $g$ such that the calculated energy levels match the measured ones. For accurate values we use the first four levels of the qubit.

| | Qubit 1 | Qubit 2 | Qubit 3A | Qubit 3B |
|---|---|---|---|---|
| $E_J$ GHz | 10.567 | 13.2821 | 18.1362 | 28.9427 |
| $E_C$ MHz | 312.75 | 303.0 | 329.8 | 309.05 |
| $g$ MHz | 202.7 | 187.0 | 192.0 | 213.8 |
| $\nu_{ge}$ GHz | 4.779 | 5.341 | 6.552 | 8.086 |
| $T1_{ge}$ $\mu s$ | 9.7 | 9.2 | 14.7 | 7.0 |
| $T2_{ge}$ $\mu s$ | 2.2 | 8.3 | 9.1 | 4.9 |
| $\nu_{ef}$ GHz | 4.411 | 4.989 | 6.180 | 7.776 |
| $T1_{ef}$ $\mu s$ | 18.4 | n.m. | 8.2 | 11.3 |
| $T2_{ef}$ $\mu s$ | 1.6 | 0.9 | 2.0 | 2.7 |

Table 2: Parameters we obtained from the characterization of the 4 qubits.

## 3.4 Two qubit experiment

Qubits 3A and 3B (Here after denoted as qubits A and B) were fabricated on the same chip with 6mm separation. The spectrum of this two qubit sample is show in Figure 32. We used it to do two qubit experiments starting with a state tomography. Because our qubits are significantly larger than in the 2D

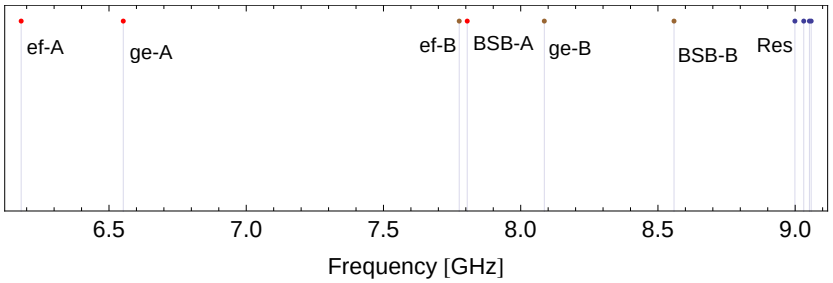


Figure 32: The spectrum of a 2 qubit sample in a 3D cavity. Red dots are for Qubit A transitions, brown for qubit B and the resonator frequencies for the qubit states $|gg\rangle, |eg\rangle, |ge\rangle$ and the bare cavity are blue.

case we consider their mutual coupling and use it to implement a controlled-Z gate. Then we look at the BSB in this sample and in an attempt to implement a CNOT gate.

### 3.4.1 Two qubit state-and process tomography

Analogous to the one qubit case, we can manipulate on the two qubit state and measure it with state tomography as described in Section 3.3.7. In Figure 33 we see the measured density matrix when the state $|ge\rangle$ was prepared with fidelity of $F_2 = 98\%$.

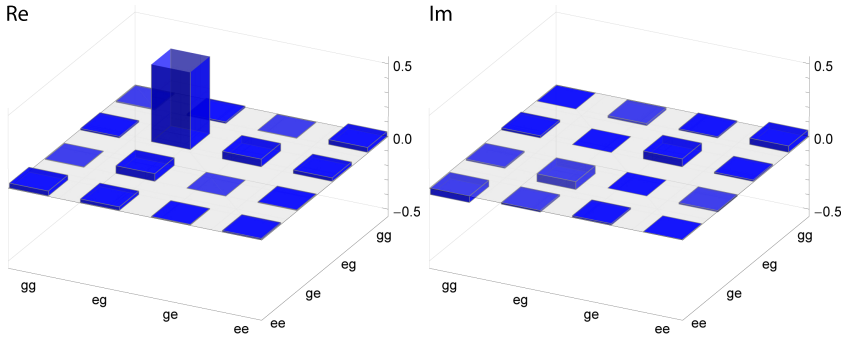


Figure 33: Two qubit state tomography was used to reconstruction of the density matrix of the $|ge\rangle$ state with fidelity $F_2 = 0.98$.

Just as state tomography is used to recover a quantum state we can expand-

ing the procedure to an operation $\mathcal{E}$. In process tomography the effect of an operation $\mathcal{E}(\rho) = \sum_i E_i \rho E_i^\dagger$ is recovered [35]. Here $E_i$ is a (non-unique) set of operators. To be able to recover $\mathcal{E}$ from measurements we linearly decompose the operators $E_i$ into a basis of fixed operators $\tilde{E}_i$,

$$E_i = \sum_m e_{im} \tilde{E}_m. \tag{3.4}$$

We can then write the operation as

$$\mathcal{E}(\rho) = \sum_{n,m} \tilde{E}_m \rho \tilde{E}_n^\dagger \chi_{nm}, \tag{3.5}$$

where $\chi_{nm} = \sum_i e_{im} e_{in}^*$ are the entries of a positive Hermitian matrix called the $\chi$ matrix .

Experimentally we get the $\chi$ matrix by staying in the computational basis $|gg\rangle, |eg\rangle, |ge\rangle, |ee\rangle$ and setting $E_i \in \{\mathbb{1}, \sigma_x, \sigma_y, \sigma_z\}$. As in the single qubit state tomography we prepare all combinations $|g\rangle, |e\rangle, \frac{1}{\sqrt{2}}(|g\rangle + |e\rangle), \frac{1}{\sqrt{2}}(|g\rangle + i|e\rangle)$ of the two qubits and perform the operation $\mathcal{E}$ each time. The resulting state is then determined with state tomography.

### 3.4.2 Qubit-qubit coupling

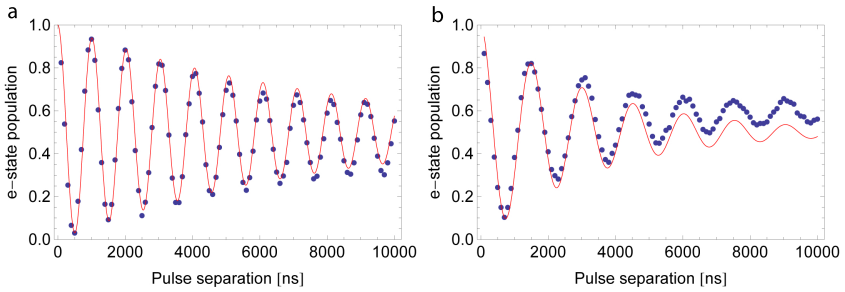


Figure 34: Ramsey oscillations on qubit b. a) Qubit A is in the ground state. b) Qubit A is in the excited state. Exciting qubit A lowers qubit B by 322kHz.

We first look at two qubit interaction via the qubit-qubit interaction. We performe a Ramsey experiment on qubit B while red detuned. In Figure 34 we see Ramsey oscillations on qubit B with qubit A in the ground state. Figure 34 b shows Ramsey oscillations on qubit B with qubit A in the excited state. The oscillations are slower when the qubit A is in the excited state than when it is in the ground state. This was done on both qubits and revealed that the qubits transition frequency was on one qubit lowered by $\delta_{qq} = 322$ kHz when the other one is excited.

From the qubit-qubit analysis above we note that a relative phase between the qubits after a time T is $\phi = 2\pi T \delta_{qq}$. By using the fixed coupling to gain

a phase $\phi = \pi$ we can implement a controlled-Z gate by waiting 1.553 $\mu s$. We perform process tomography by preparing the various states as described above, wait for 1.553 $\mu s$ and then perform state tomography. We obtain a $\chi$ matrix as shown in Figure 35 and a process fidelity of $F_2 = 67\%$.

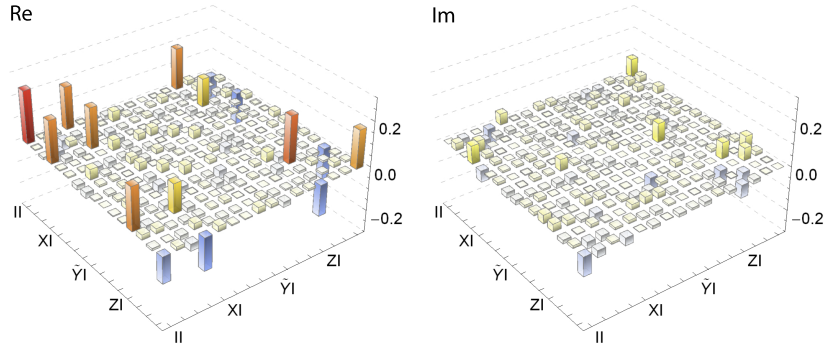


Figure 35: The real part, a), and imaginary part, b), of the controlled-Z $\chi$ matrix. The controlled-Z gate implemented here used the fixed qubit-qubit coupling.

The presence of fixed coupling is naturally problematic when not wanted. A CNOT(or controlled-Z) gate one can turn on and off is therefore desirable.

### 3.4.3 Controlled-NOT gate

An implementation of a CNOT gate was proposed by Saito [45] using blue sideband pulses. The scheme is shown in Figure 36.

We will first describe the controlled-Z gate, $U_{CZ}$, which induces a $\pi$ phase on the $|eg\rangle$ state as shown in Table 3 (notation: $|TC\rangle$ or $|TCn\rangle$ where $|T\rangle$ is the target qubit, $|C\rangle$ is the control qubit and $|n\rangle$ is the photon number). If the control qubit $|C\rangle$ is in the excited state no BSB transition is driven and no phase accumulates on the target qubit $|T\rangle$. If $|C\rangle$ is in the ground state and we set our drive to the frequency

$$\omega_d = \frac{\omega_{\mathrm{r}} - 2\chi_{\mathrm{C}} + \omega_{\mathrm{geC}}}{2}. \tag{3.6}$$

Here where $\omega_{\mathrm{r}}$ is the resonator frequency with the qubit in the ground state, $2\chi_C$ is the dispersive shift of the resonator due to the control qubit and $\omega_{\mathrm{geC}}$ is the transition frequency of the control qubit. The BSB transition $|gg0\rangle \rightarrow |ge1\rangle$ is now driven on-resonance and accumulate no phase in the $|ge1\rangle$ state. If the target qubit is excited the resonator will shifted by $2\chi_T$. If we drive at the BSB transition $|eg0\rangle \rightarrow |ee1\rangle$ in the same rotating frame as when $|T\rangle$ is in the ground state we accumulate a phases, $\phi$ while in the $|ee1\rangle$ state for a time T $\phi = \mathrm{T}\chi_T$(the 2 is not there because it is a two photon process). By adjusting the time T we can get a $\pi$ phase on the $|ee1\rangle$ state while accumulating no phase on

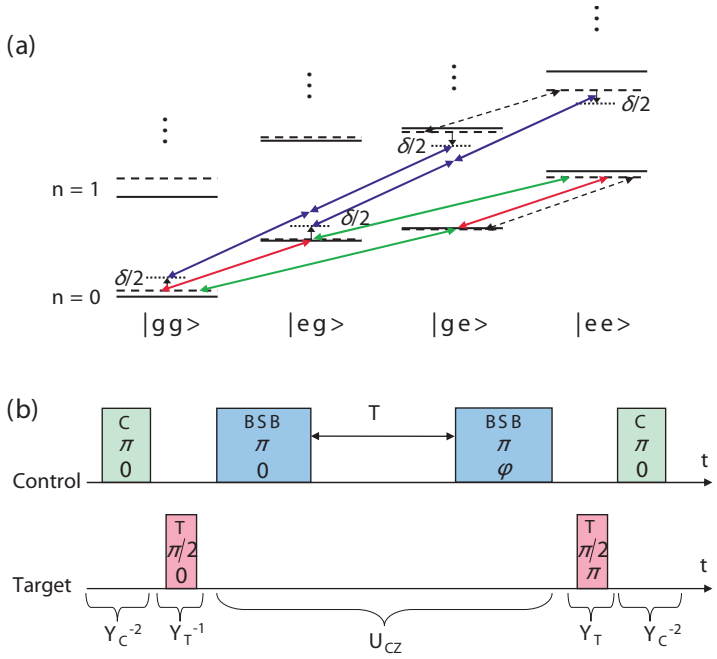


Figure 36: a) An energy level diagram for the two qubit system in the 0 and 1 photon state of the resonator. The solid lines are the undressed states, the coursely dashed levaes are the dispersively shifted levels and the fine dashed levels invlude the ac-Stark shift $\delta$ of the drive. The arrows are color coded to match the pulse sequence. b) A pulse diagram for the implementation of a CNOT gate. It consists of a blue sideband based controlled-Z gate $U_{\mathrm{CZ}}$ (blue), a Hadamard gate on the target qubit $\mathrm{Y_T}$(red) and two $\pi$ pulses on the control qubit $\mathrm{Y_C}$(green).

the other states $|ge1\rangle$, $|ge0\rangle$ and $|ee0\rangle$. To complete the controlled-Z gate apply a second BSB pulse to bring the n=1 states back to the n=0 states. As stated in Section 2.7, applying Hadamard gates on the target qubit of a controlled-Z gate, as shown in Figure 36 b (red), gives us a CNOT gate. The outermost pi pulses on the control qubit, see (Figure 36 b (green), add up to $2\pi$ and only affects the scheme such that the target qubit is flipped when the control qubit is in the excited state.

In this idealized outline of the CNOT scheme the length of the pulses is assumed to be negligible in comparison to T. We have also not taken into account the phase effect the ac-Stark shift from the drive $\delta$ nor the implementation of driving an offset BSB transition. In Ref. [45] it is suggested to apply a phase $\phi_\delta = \pi T\delta$ on the second BSB pulse to correct for the phase effect of the ac-Stark shift. We however do not have phase control on our BSB pulses such that

$\phi_\delta = 0$. The non-zero pulse lengths and off-resonant BSB transition we will discuss in the following sections.

$$\begin{array}{rcl} |gg\rangle & \rightarrow & |gg\rangle \\ |eg\rangle & \rightarrow & -|eg\rangle \\ |ge\rangle & \rightarrow & |ge\rangle \\ |ee\rangle & \rightarrow & |ee\rangle \end{array}$$

Table 3: The effect of $U_{CZ}$ on the states in the computational basis.

### 3.4.4 Optimizing the blue sideband

In order to minimize the state preparation time we want to maximize the power used on the sidebands. Due to the close proximity of qubit B's $\nu_{ge}$ transition to both sidebands we tested the effect of the BSB drives on qubit B, The test schems are depicted in Figure 37. The second $\pi$ pulse on qubit A has to do with more efficient qubit readout.

By doing a $\pi$ pulse we excite the qubit such that the following pulse at the BSB frequency does not drive the transition. We will still refer to it as the BSB pulse. The influence of this tone on qubit B is thus only that of an off-resonant but strong drive. Subsequent to the BSB pulse we perform a Ramsey experiment on qubit B. The BSB drive powers were varied and the pulse lengths were chosen such that at least a $\pi$ rotation would have been driven on the sidebands if the qubit was in the ground state.

In Figure 38 a we see Ramsey oscillations which are not drastically affected by a 500ns BSB A pulse at 4.3 dBm output power of the microwave generator.

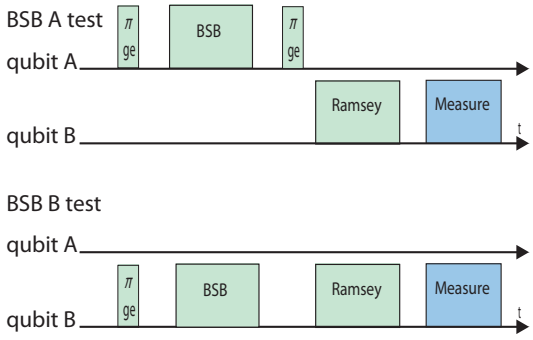


Figure 37: The figure shows the pulse sequences used to test how qubit B is affected by the strong BSB drive tones. The $\pi$ pulse in the begining of the sequneces prevents the BSB transition from being driven. The effect is measured by performing a Ramsey experiment on qubit B

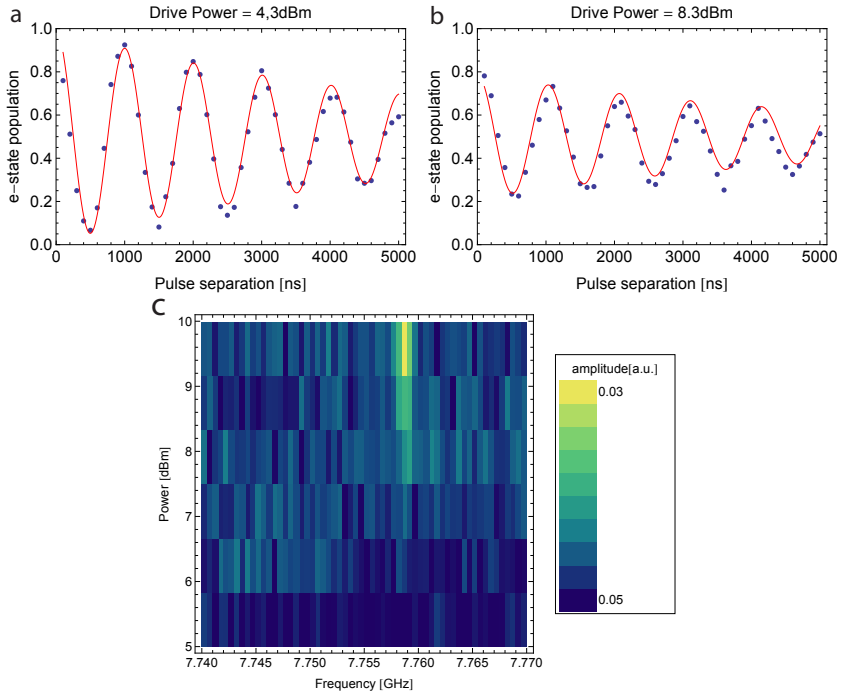


Figure 38: Ramsey oscillations on qubit B after a BSB pulse on qubit A at a) 4.3 dBm , b) 8.3dBm. Spectroscopy on the BSB on qubit A varying the spectroscopy drive power.

In Figure 38 b output power has been increased to 8.3 dBm and we observe a diminished ampliude of the Ramsey oscillations. If we however look at Figure 38 c we see that the minimum power needed to drive BSB A is around 9 dBm. We thus conclude that we can not use BSB A.

The test for BSB on qubit B requires a 100 ns pulse length. We find the maximal power to be 10 dBm without diminishing the amplitude of Ramsey oscillations, see Figure 39 a), b) and c). We however choose to drive at 14 dBm to get a higher Rabi frequency.

Proceeding with the BSB on qubit B we note that the BSB resonance frequency is lowered by $\chi_A$ when qubit A is in the excited state. This is the dispersive shift of the resonator as described in previously in Section 3.4.3.

We performed Rabi experiments on BSB B at 14 dBm for various frequencies, both with qubit A in the excited and the ground state, see Figure 40 a. By fitting the date with parabolas for both states of qubit A we find the BSB frequencies to be 8.5467 GHz when qubit A is excited and 8.5495 GHz when it is in the ground state i.e. a difference of 2.8 MHz. The Rabi frequencies were 5.43 MHz and 5.48 MHz for the excited and the ground state respectively. In order to drive the BSB transition regardless of the state of qubit A we set the frequency

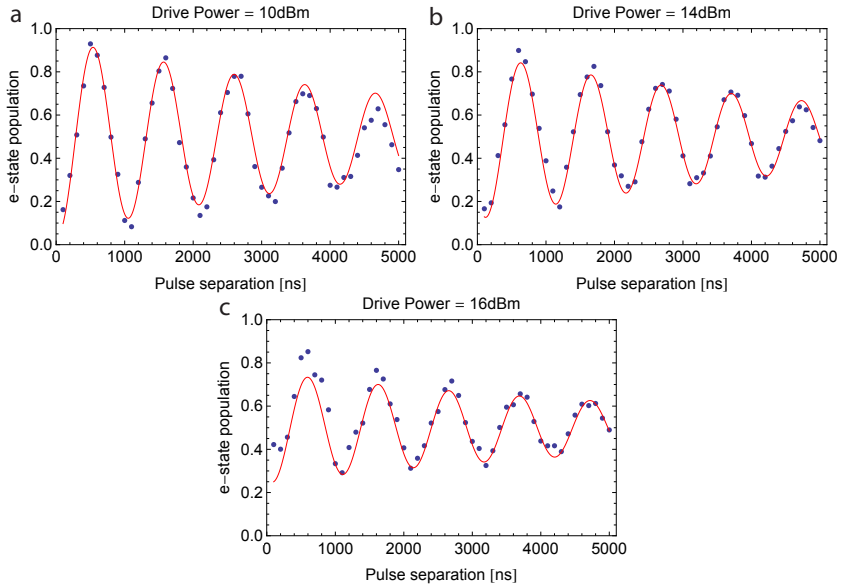


Figure 39: Ramsey oscillations on qubit B following a strong tone at the BSB frequency of qubit B at a) 10 dBm, b) 14 dBm, c) 16 dBm.

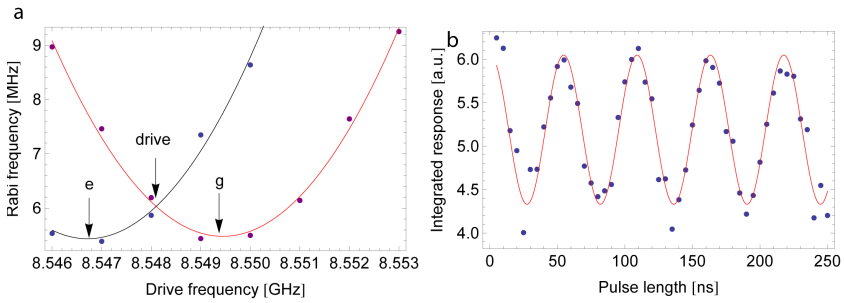


Figure 40: a) Rabi frequency of the BSB transition of qubit B varying the BSB drive frequency. The purple dots(measured) and the red line (fit) represent the BSB Rabi frequency when qubit A is in the ground state and the blue dots(measured) and black line(fit) represent the BSB frequency when the qubit is in theescited state. We drive the BSB transition at the intersection of the black and the red lines where the Rabi frequency is the same for both states of the qubit. b) On-resonance Ramsey oscillations on the BSB is used to measure the ac-Stark shift caused by the drive.

to the intersection of the two parabolas in Figure 40, at $\nu_d = 8.54808$ GHz, where the Rabi rate is the same for both cases. This however means that the detuning from resonant transitions is roughly 1/3 of the Rabi frequency. In the Bloch sphere picture such a detuning compared to the Rabi rate results in a

rotation of the Bloch vector about an axis with an 18 degree angle from the horizontal plane. Considering the projection of the Bloch vector onto the z axis of the Bloch sphere we see that the population of the $|e1\rangle$ state can maximally reach 90%. Having found the BSB resonances with Rabi experiments we can measure the ac-Stak shift $\delta$ from the drive. When performing an on-resonance Ramsey experiment at the BSB resonance we note that the shift is not present during the time between the $\pi/2$ pulses. This effectively gives us a detuning which amounts to the ac-Stark shift from the drive. The Ramsey oscillations from such an experiment is shown in Figure 40 b. The frequency is twice the detuning in this case because it is a two photon process. We measured the Stark shift of the BSB B transition when driven at 14 dBm to be 9.2MHz. When we take that shift into account the measured BSB frequency matches the theoretical frequency $\frac{\omega ge+\omega_r}{2(2\pi)} = 8.5586$ GHz.

### 3.4.5 Phase evolution

By driving at $\nu_d = 8.54808$ GHz we wanted to see if we could still, despite not having phase control and a high Rabi rate on the BSB, implement a controlled-Z gate based on the Saito scheme. To investigate that we performed four phase Ramsey schemes, shown in Figure 41, where were we map the phase evolution of our qubits. A phase Ramsey consists of two $\pi/2$ pulses separated by time $\tau$

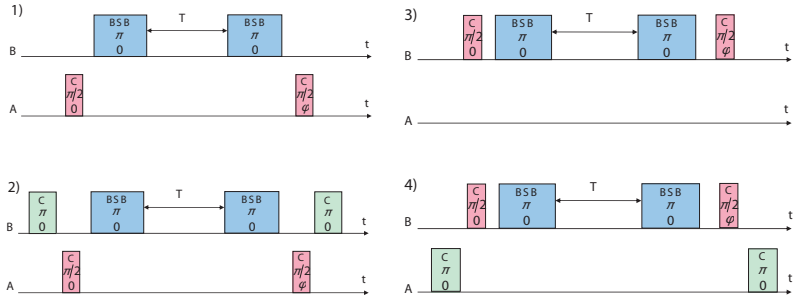


Figure 41: The pulse patterns used to map the phase evolution of the qubits when two BSB $\pi$ pulses, separated by a varying time T, are applied on qubit B. Patterns 1 and 2 phase map qubit B and patterns 3 and 4 phase map qubit A.

as in the usual Ramsey experiment. The difference is that in a phase Ramsey experiment $\tau$ is constant but the phase of the second $\pi/2$ pulse is varied. In our case we want to do a phase Ramsey on both qubits, A and B, while implementing the BSB pulses in the Saito scheme in between the $\pi/2$ pulses. The time T, between the BSB pulses, plus the pulse lengths themselves must be within the time $\tau$. We can vary T to see how the phase on qubit evolves. The pahse mapping on each qubit is performed with the alternative one both in the ground state and the excited state. This we did for T=0-40 ns and three periods of the

phase for each pattern, see Figure 42. We can see loss of contrast in the phase

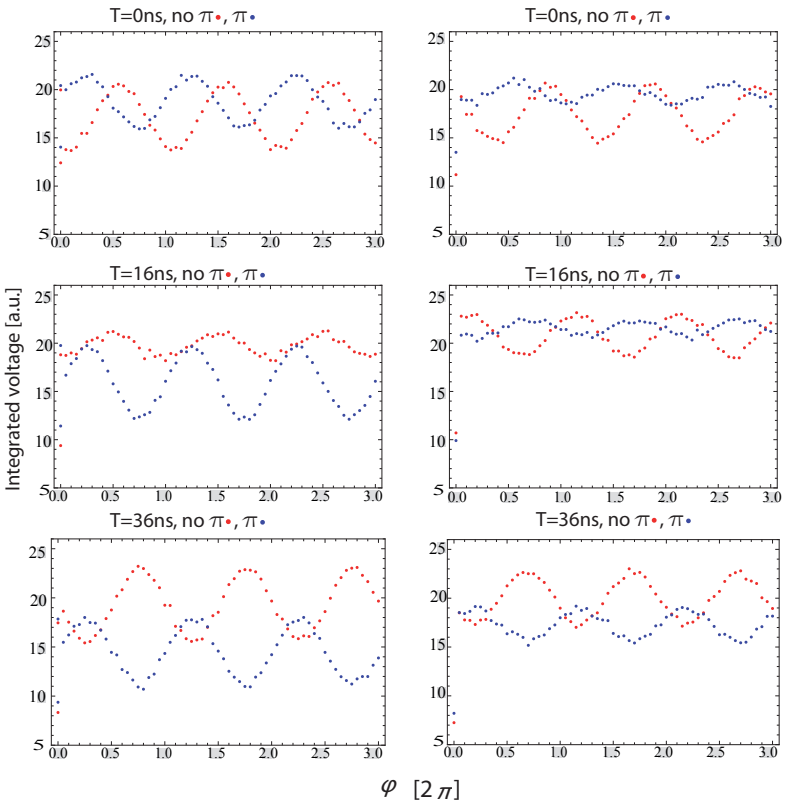


Figure 42: Phase Ramsey oscillations for 0, 16 and 36 ns are shown. We see the contrast diminish and the cavity transmission signal get higher for $T = 16$ ns. The contrast improves again for $T = 36$ ns.

Ramsey oscillations for times at 16 ns. This is due to the phase acquired from the ac-Stark shift of the drive such that the second BSB pulse rotates the Bloch vector about itself.

What we ideally need is to find a time T such that the phase Ramsey oscillations on qubit B, i.e. from patterns 1 and 2, are $\pi$ out of phase and that the phase Ramsey oscillations on qubit A, from patterns 3 and 4, are mutually in phase and with either 1 or 2. We plot the phases of the fits to the various patterns in Figure 43 to see the its dependance on T.

The phases from pattern 2 and 3 behave as expected. Because we excite qubit B in pattern 2 the BSB transition cannot be driven and the cause no

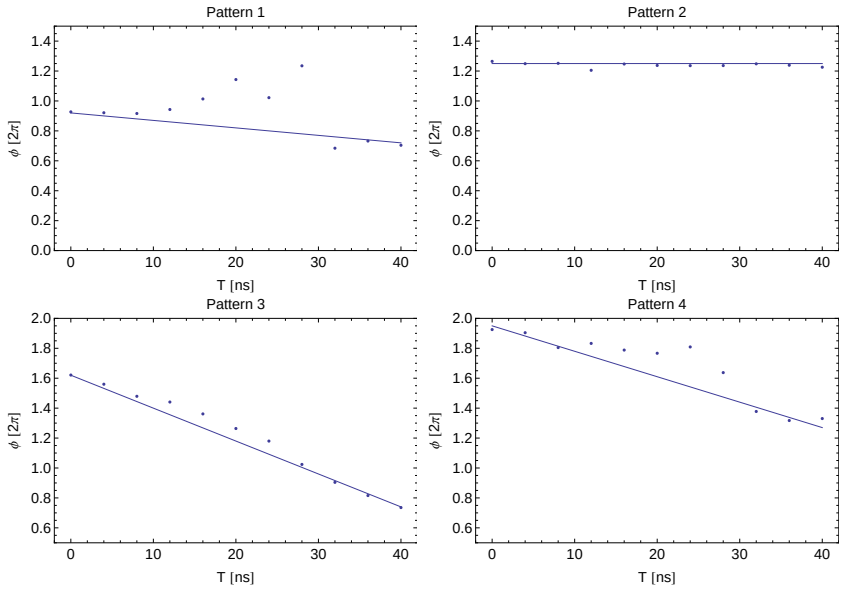


Figure 43: The phases from patterns 1, 2, 3 and 4 for T= 0-40 ns. The behaviour is as expected for patterns 2 and 3 i.e. static and linear. In the case of patterns 1 and 4 we cannot account for the non-linearity. Both patterns 1 and 4 drive the BSB with qubit A excited.

additional phase is accumulation. In pattern 3 we let the phase accumulate for varying time, T, leading to a linear phase dependence. For patterns 1 and 4 we have no clear relation between the time T and the phase. We notice now that in patterns 2 and 3 the sideband transition is either not driven or driven with qubit A in the ground state. In patterns 1 and 4 the excited or a superposition state of qubit A affects the BSB transition. This suggests that the BSB transition is not being driven coherently in the case qubit A is not in the ground state.

# 4 Conclusions

We successfully developed a 3D cavity resonator with a quality factor of 2 million in a dilution refrigerator at 20mK with magnetic shielding. The various alloys tested without a magnetic shield only reached a Q-factor of about 100000 indicating strongly its necessity for higher Q-factors. A full geometry modeling of the cavity predicted a value of the fundamental resonance frequency which was within the reproducibility accuracy of the measured cavities. It also predicted cavity transmission dependance on the length of the cavity coupling pins close to teh measured values. In addition we note that the measured and the simulated frequencies of the first mode differ from the text book rectangular cavity frequency of the same dimensions only by 50 MHz.

We characterized 4 qubits with T1 and T2 of up to 14 $\mu s$ and 9.7 $\mu s$ for the first excited state respectively. Surprisingly we observed a 18 $\mu s$ T1 for a second excited state and a T2 of 2.7 $\mu s$. We performed both single tone and two tone BSB transitions. For the single tone case we observed an ac-Stark shift of the BSB transition towards lower frequencies. By driving Rabi oscillations at various drive frequencies frequency the resonant frequency could be determined from the lowest Rabi rate. The Stark shift could then be measured with an on-resonance Ramsey experiment. With two qubits in the resonator we observed direct coupling between the two qubits of 322 kHz and used it to implement a cphase gate with 67% process fidelity. We made an effort to implement a CNOT gate using one blue sideband. The scheme could not be realized due to both restrictions on the BSB phase control and BSB Rabi rate limitations of the sample. We however probed the phase evolution of the qubits under the operation of the CNOT protocal without phase correction to see if a slightly alternative implementation could still be successfull. We found that the shifted BSB transition did not behave as we expected such that the CNOT gate was not nicely implemented.

The next step for implementing the CNOT gate would be to have phase control on the BSB transition. In our two qubit sample one sideband transition rate reaches an upper limit due to the vicinity of the qubit frequency to the resonator. A qubit with a lower excitation frequency would thus enable faster BSB transition. The implementation of local qubit control and qubit tunability would allow qubit manipulation with vacuum Rabi oscillations and open up a wider range of experiments achievable in 3D cavities. Further experiments and technical implementations, such as shielding and cable termalization, can be done to reduce noise in the cavities and prolong lifetimes. Developing cavities with lifetimes of hundreds millions or more are known from particle physics. Such cavities could be tested as possible memories for quantum information.

# 5 Aknowledgements

I would like to thank Prof. Dr. Andreas Wallraff first of all for allowing me to do this project in his group. In addition for guiding comments and discussions during this whole period.

I am very grateful to Dr. Johannes Fink for his supervision and showing me how one approaches such a sophisticated physics experiment. He mentored me on circuit QED with superconducting circuits, dilution refrigerators and numerous aspects of experimental physics. His support also involved helping me keep my eye on the ball and focus on getting things done.

The guidance of Marek Pechal through the jungle of Cleansweep, our qubit measurement program, and how one actually implements the experiments was very enjoyable and informative. His theoretical knowledge of circuit QED was also a very helpful.

When dealing with blue sideband transitions and tomography I was fortunate to be able to consult with Matthias Baur and benefit from his vast knowledge of the subjects. Joonas Govenius and Simon Berger showed me how to calibrate mixers and Lars Steffen was always so kind to help me with all sorts of computer related problems.

Last but not least, I would like to thank my family for their company and support. A special thanks to the my uncle and aunt, Nonni and Hilma and the whole gang at Rebmooswe 11 for taking me in and putting up with the occasional “kidnapping”.

# References


[1] Hanhee Paik, D. I. Schuster, Lev S. Bishop, G. Kirchmair, G. Catelani, A. P. Sears, B. R. Johnson, M. J. Reagor, L. Frunzio, L. I. Glazman, S. M. Girvin, M. H. Devoret, and R. J. Schoelkopf. Observation of high coherence in josephson junction qubits measured in a three-dimensional circuit qed architecture. *Phys. Rev. Lett.*, 107:240501, Dec 2011.

[2] A. M. Turing. On computable numbers, with an application to the entscheidungsproblem. *Proceedings of the London Mathematical Society*, s2-42(1):230–265, 1937.

[3] R. P. Feynman. Simulating physics with computers. *International Journal of Theoretical Physics*, 21(6):467–488, June 1982.

[4] D. Deutsch. Quantum theory, the Church-Turing principle and the universal quantum computer. *Proceedings of the Royal Society of London. Series A, Mathematical and Physical Sciences*, 400(1818):97–117, July 1985.

[5] P. W. Shor. Algorithms for quantum computation: Discrete logarithms and factoring. In *Proceedings, 35th Annual Symposium on Foundations of Computer Science, Santa Fe*, page 124. IEEE Computer Society Press, 1994.

[6] Lov K. Grover. A fast quantum mechanical algorithm for database search. In *Proceedings of the twenty-eighth annual ACM symposium on Theory of computing*, pages 212–219, Philadelphia, Pennsylvania, United States, 1996. ACM.

[7] Lieven M. K. Vandersypen, Matthias Steffen, Gregory Breyta, Costantino S. Yannoni, Mark H. Sherwood, and Isaac L. Chuang. Experimental realization of Shor's quantum factoring algorithm using nuclear magnetic resonance. *Nature*, 414:883, 2001.

[8] D. P. Di Vincenzo. Quantum computation. *Science*, 270:255, 1995.

[9] L. M. K. Vandersypen and I. L. Chuang. Nmr techniques for quantum control and computation. *Rev. Mod. Phys.*, 76:1037, 2004.

[10] Ronald Hanson and David D. Awschalom. Coherent manipulation of single spins in semiconductors. *Nature*, 453(7198):1043–1049, June 2008.

[11] L. Jiang, J. S. Hodges, J. R. Maze, P. Maurer, J. M. Taylor, D. G. Cory, P. R. Hemmer, R. L. Walsworth, A. Yacoby, A. S. Zibrov, and M. D. Lukin. Repetitive Readout of a Single Electronic Spin via Quantum Logic with Nuclear Spin Ancillae. *Science*, 326(5950):267–272, 2009.

[12] Pieter Kok, W. J. Munro, Kae Nemoto, T. C. Ralph, Jonathan P. Dowling, and G. J. Milburn. Linear optical quantum computing with photonic qubits. *Rev. Mod. Phys.*, 79(1):135–174, Jan 2007.

[13] I. Marcikic, H. de Riedmatten, W. Tittel, H. Zbinden, and N. Gisin. Long-distance teleportation of qubits at telecommunication wavelengths. *Nature*, 421(6922):509–513, 2003.

[14] Thomas Monz, Philipp Schindler, Julio T. Barreiro, Michael Chwalla, Daniel Nigg, William A. Coish, Maximilian Harlander, Wolfgang Hänsel, Markus Hennrich, and Rainer Blatt. 14-qubit entanglement: Creation and coherence. *Phys. Rev. Lett.*, 106:130506, Mar 2011.

[15] Y. Nakamura, Y. A. Pashkin, and J. S. Tsai. Coherent control of macroscopic quantum states in a single-cooper-pair box. *Nature*, 398(6730):786–788, April 1999.

[16] A. Blais, R.-S. Huang, A. Wallraff, S. M. Girvin, and R. J. Schoelkopf. Cavity quantum electrodynamics for superconducting electrical circuits: An architecture for quantum computation. *Phys. Rev. A*, 69(6):062320, June 2004.

[17] A. Wallraff, D. I. Schuster, A. Blais, L. Frunzio, R.-S. Huang, J. Majer, S. Kumar, S. M. Girvin, and R. J. Schoelkopf. Strong coupling of a single photon to a superconducting qubit using circuit quantum electrodynamics. *Nature*, 431:162–167, 2004.

[18] A. Wallraff, D. I. Schuster, A. Blais, L. Frunzio, J. Majer, S. M. Girvin, and R. J. Schoelkopf. Approaching unit visibility for control of a superconducting qubit with dispersive readout. *Phys. Rev. Lett.*, 95:060501, 2005.

[19] J. Johansson, S. Saito, T. Meno, H. Nakano, M. Ueda, K. Semba, and H. Takayanagi. Vacuum Rabi oscillations in a macroscopic superconducting qubit LC oscillator system. *Phys. Rev. Lett.*, 96(12):127006, 2006.

[20] Yifu Zhu, Daniel J. Gauthier, S. E. Morin, Qilin Wu, H. J. Carmichael, and T. W. Mossberg. Vacuum rabi splitting as a feature of linear-dispersion theory: Analysis and experimental observations. *Phys. Rev. Lett.*, 64(21):2499, May 1990.

[21] A. Wallraff, D. I. Schuster, A. Blais, J. M. Gambetta, J. Schreier, L. Frunzio, M. H. Devoret, S. M. Girvin, and R. J. Schoelkopf. Sideband transitions and two-tone spectroscopy of a superconducting qubit strongly coupled to an on-chip cavity. *Phys. Rev. Lett.*, 99:050501, 2007.

[22] P. J. Leek, S. Filipp, P. Maurer, M. Baur, R. Bianchetti, J. M. Fink, M. Göppl, L. Steffen, and A. Wallraff. Using sideband transitions for two-qubit operations in superconducting circuits. *Phys. Rev. B*, 79:180511, 2009.

[23] L. DiCarlo, M. D. Reed, L. Sun, B. R. Johnson, J. M. Chow, J. M. Gambetta, L. Frunzio, S. M. Girvin, M. H. Devoret, and R. J. Schoelkopf. Preparation and measurement of three-qubit entanglement in a superconducting circuit. *Nature*, 467:574–578, 2010.

[24] A. Fedorov, L. Steffen, M. Baur, M. P. da Silva, and A. Wallraff. Implementation of a toffoli gate with superconducting circuits. *Nature*, 481(7380):170–172, jan 2012.

[25] John Clarke and Frank K. Wilhelm. Superconducting quantum bits. *Nature*, 453(7198):1031–1042, June 2008.

[26] Lars Steffen. Local qubit control in circuit quantum electrodynamics. Master's thesis, Laboratory of solid state physics, ETH Zurich, 2008.

[27] David K. Cheng. *Field and Wave Electrodynamics*. Addison-Wesley, 1992.

[28] Johannes Fink. *Quantum nonlinearities in strong coupling circuit QED*. PhD thesis, ETH Zurich, 2010.

[29] D. M. Pozar. *Microwave Engineering*. Addison-Wesley Publishing Company, 1993.

[30] Kajfez. Q factor measuremets, analog and digital. Website, 04 2012.

[31] M. H. Devoret, A. Wallraff, and J. M. Martinis. Superconducting qubits: A short review. *cond-mat/0411174*, -, 2004.

[32] R.P. Feynman, M. Sands, and R.B. Leighton. *The Feynman Lectures on Physics Vol.3*. Addison-Wesley, 1971.

[33] V. Bouchiat, D. Vion, P. Joyez, D. Esteve, and M. H. Devoret. Quantum coherence with a single Cooper pair. *Phys. Scr.*, T76:165–170, 1998.

[34] Jens Koch, Terri M. Yu, Jay Gambetta, A. A. Houck, D. I. Schuster, J. Majer, Alexandre Blais, M. H. Devoret, S. M. Girvin, and R. J. Schoelkopf. Charge-insensitive qubit design derived from the Cooper pair box. *Phys. Rev. A*, 76(4):042319, 2007.

[35] Michael A. Nielsen and Isaac L. Chuang. *Quantum Computation and Quantum Information*. Cambridge University Press, 2000.

[36] E.T. Jaynes and F.W. Cummings. Comparison of quantum and semiclassical radiation theories with application to the beam maser. *Proceedings of the IEEE*, 51(1):89–109, 1963.

[37] A. Blais, J. Gambetta, A. Wallraff, D. I. Schuster, S. M. Girvin, M. H. Devoret, and R. J. Schoelkopf. Quantum-information processing with circuit quantum electrodynamics. *Phys. Rev. A*, 75(3):032329, March 2007.

[38] F. Pobell. *Matter and Methods at Low Temperatures*. Springer, 3rd edition,, 2006.

[39] Simon Schmidlin. Generation of amplitude and phase controlled microwave pulses for qubit manipulation in circuit qed. Master's thesis, Laboratory for Solid State Physics, ETH Zurich, 2009.

[40] M. D. Reed, L. DiCarlo, B. R. Johnson, L. Sun, D. I. Schuster, L. Frunzio, and R. J. Schoelkopf. High-fidelity readout in circuit quantum electrodynamics using the jaynes-cummings nonlinearity. *Phys. Rev. Lett.*, 105(17):173601, Oct 2010.

[41] Lev S. Bishop, Eran Ginossar, and S. M. Girvin. Response of the strongly driven jaynes-cummings oscillator. *Phys. Rev. Lett.*, 105(10):100505, Sep 2010.

[42] Maxime Boissonneault, J. M. Gambetta, and Alexandre Blais. Improved superconducting qubit readout by qubit-induced nonlinearities. *Phys. Rev. Lett.*, 105(10):100504, Sep 2010.

[43] D. I. Schuster, A. Wallraff, A. Blais, L. Frunzio, R.-S. Huang, J. Majer, S. M. Girvin, and R. J. Schoelkopf. AC Stark shift and dephasing of a superconducting qubit strongly coupled to a cavity field. *Phys. Rev. Lett.*, 94(12):123602, April 2005.

[44] D. I. Schuster, A. A. Houck, J. A. Schreier, A. Wallraff, J. M. Gambetta, A. Blais, L. Frunzio, J. Majer, B. Johnson, M. H. Devoret, S. M. Girvin, and R. J. Schoelkopf. Resolving photon number states in a superconducting circuit. *Nature*, 445(7127):515–518, February 2007.

[45] Shiro Saito, Todd Tilma, Simon J. Devitt, Kae Nemoto, and Kouich Semba. Experimentally realizable controlled not gate in a flux qubit/resonator system. *Phys. Rev. B*, 80(22):224509–, December 2009.